POLITECNICO DI MILANO

Corso di Laurea Magistrale in Ingegneria Aeronautica

Scuola di Ingegneria Industriale e dell'Informazione

Dipartimento di Scienze e Tecnologie Aerospaziali

A model for in-flight ice accretion based on the exact solution of the unsteady Stefan problem

Relatore: Prof. Alberto GUARDONE

Co-relatori: Ing. Giulio GORI
Ing. Marta ZOCCA

Tesi di laurea di:
Gianluca Parma
Matr. 801695

Anno Accademico 2014 - 2015

Abstract

An accurate modelling of icing phenomena is fundamental in aeronautical applications for both aircraft design and for the in-flight safety. During the past years, a number of icing models have been developed in order to perform accurate icing simulations to reduce the costs of wind tunnel testing. Unfortunately, in-flight icing modeling still presents some limitations. In the present work, a new unsteady model based on the exact unsteady solution of the Stefan problem is derived for the first time to assess the influence of the unsteadyness of the temperature profile within the ice layer on ice accretion. A local correction to the air temperature is also included to account for the dependence of the outer (air) temperature on the flow field. A novel mesh deformation procedure was also developed and implemented in the PoliMIce suite, which is based on the Shepard interpolation method. Numerical simulations of two-dimensional airfoil in icing conditions were carried out to assess the correctness of the new model and its behavior in rime and glaze ice conditions. Numerical simulations relied upon the open-source `OpenFOAM` suite for the computation of the aerodynamic flow field and of the droplet trajectories. Simulations performed in Ch. 5 showed that the contributions of the unsteady terms is not significant in the considered cases, apart from an initial transitory. In this lapse, the derivative of the temperature at the wall is higher than the one calculated by the Myers model. This behavior is possibly important in the design of an anti-icing system for the evaluation of the heat flux to apply at the wall. On the other hand, the introduction of the local temperature gives more accurate results in the ice shape prediction. In the rime ice case, the occurrence of the characteristic horn structures is observed and the ice thickness at the stagnation point is found to be closer to the experimental one.

Keywords: ice, icing models, Myers, Stefan problem, exact solution, unsteady problem, similarity solution, mesh deformation, Shepard, PoliMIce, OpenFOAM.

Sommario

Un'accurata modellazione dei fenomeni di formazione di ghiaccio in applicazioni aeronautiche è di fondamentale importanza sia per la progettazione di nuovi aeromobili, sia per garantirne la sicurezza in volo. Durante gli anni passati sono stati proposti modelli di previsione del ghiaccio sempre più accurati ma che mostrano tutt'ora alcune limitazioni. In questo lavoro di tesi viene proposto e discusso un nuovo modello di previsione della formazione del ghiaccio basato sulla soluzione esatta instazionaria del problema di Stefan per mezzo di un approccio in similitudine. A differenza dei modelli già esistenti in cui gli scambi termici sono calcolati usando il valore di temperatura all'infinito a monte, in questo lavoro, anche per le simulazioni incomprimibili, viene definito e ricostruito il campo di temperatura locale vicino alla parete utilizzando le relazioni isoentropiche. Viene inoltre sviluppato e implementato un nuovo deformatore di griglia per il software `PoliMIce` basato sull'algoritmo di interpolazione di Shepard.

I casi test presi come riferimento nel Ch. 5 per verificare le novità proposte sono stati scelti in modo da comprendere sia situazioni dominate dal ghiaccio rime, che situazioni dominate dal ghiaccio glaze. I risultati, ottenuti mediante il software `PoliMIce` accoppiato al solutore aerodinamico `OpenFOAM`, mostrano come il rilassamento del vincolo di stazionarietà non porti a sostanziali benefici per quanto riguarda la forma finale del ghiaccio ma interessi solamente il transitorio iniziale. In questa fase si mostra come la derivata della temperatura a parete sia maggiore della stessa calcolata con l'altro modello di riferimento (modello di Myers); ciò può essere interessante da tenere in considerazione durante la progettazione di un sistema antighiaccio basato sul riscaldamento della parete. Ulteriori studi sono necessari per definire le condizioni in cui questa differenza diventa rilevante. D'altra parte, l'utilizzo del campo di temperatura locale unitamente alla modellazione del flusso di acqua superficiale, mostra un notevole miglioramento nella previsione della forma finale assunta dal ghiaccio. Nel caso di accrescimento rime si mostra come questa modifica comporti la comparsa di formazioni a "corna" e di uno spessore di ghiaccio al punto di ristagno più vicino al valore misurato sperimentalmente.

Keywords: ghiaccio, modello di accrescimento, Myers, problema di Stefan, soluzione esatta, problema instazionario, soluzione di similarità, deformazione di griglia, Shepard, PoliMIce, OpenFOAM.

Ringraziamenti

Al termine di questa esperienza di tesi vorrei innanzitutto ringraziare il prof. *Alberto Guardone* per la stimolante possibilità datami e per la sua grande disponibilità e presenza.

Un ringraziamento particolare va poi a *Marta* e *Giulio* per il loro costante supporto e la loro infinita pazienza, grazie al vostro esempio ho imparato molto e sono sempre stato spronato al meglio. Grazie anche a tutti gli amici del laboratorio, *Barbara*, *Luuc*, *Davide* e *Luca* per tutti i momenti passati insieme e per il clima di serenità e confronto che hanno sempre creato durante questi mesi.

Grazie di cuore alla mia famiglia, *mamma*, *papà* e *Chiara* per essermi sempre stati accanto e avermi saputo sostenere nei momenti più difficili, ma soprattutto per avermi sempre lasciato libero di scegliere la mia strada.

Grazie anche ai fantastici compagni di viaggio incontrati durante questi anni di università, *Ste*, *Luca*, la *Ale*, *Silvia*, *Raul*, l'*Andre*, il *Dani*, *Claudio*, *Fra*, *Pez* e *Panz*. Grazie per aver alleggerito le fatiche dello studio e per aver condiviso le gioie e le delusioni di questi anni.

Per finire un ringraziamento a tutti i sulbiatesi e agli amici scout, in particolar modo a *Jacopo*, *Andrea* e *Andrea*, *Beppe* e *Andre*.

Contents

List of Figures

List of Tables

Chapter 1

Introduction

Icing phenomenon plays a critical role in aircraft design and in aviation safety research programs.

Indeed, several reports and statistical analyses (see [12], [13], [14]) have shown how every year a non-negligible number of in-flight accidents occurs due to icing problems. Fortunately not every accident involves life loss, but some cases have been very catastrophic. For example, two of the most recent and tragic cases has been the crash of the American Eagle Flight 4184 in 1994 (68 deaths) [15] and the crash of the COMAIR Flight 3272 in 1997 (29 deaths) [16]. In the first accident an unexpected ice accretion over a wing caused a problem to the movement of an aileron and the consequent loss of control of the plane. In the second case a thin rough ice accretion over the lifting surfaces lead to a loss of control during the landing phase. In Fig. 1.1 some statistics about accidents caused by icing are shown to provide an indication of the icing risks.

In addition to these safety issues, industries are interested in icing research for economical reasons. For example, the increase of drag due to structural icing is reflected in an increase of fuel consumption and so, in costs.

For these reasons, since the 1940s several experiments have been performed to investigate the physics of structural icing and its effects on the aircraft parts (wings, probes, propellers, etc) in order to develop more effective anti-icing systems and to identify the most critical conditions during the flight. At the same time, the first theoretical approaches to the phenomenon were suggested by Hardy (1946) [17], Langmuir & Blodgett (1946) [18] and Messinger (1953) [7] who proposed the first, and still in use, model to describe the ice accretion over aircraft surfaces.

In the following years many research structures such as the *NACA* (now NASA), the *Royal Aerospace Establishment* (RAE), the *Defence Evaluation and Research Agency* (DERA), the *Office National d'Etudes et de Recherches Aérospatiales* (ONERA), the *Centro Italiano Ricerca Aerospaziale* (CIRA) and many others from different countries contributed to the creation of a wide database of experimental results and the development of various icing prediction codes.

The aim of the ice accretion codes are diverse and nowadays they represent a fundamental tool in aircraft design. They can be used to predict the ice shapes, to investigate

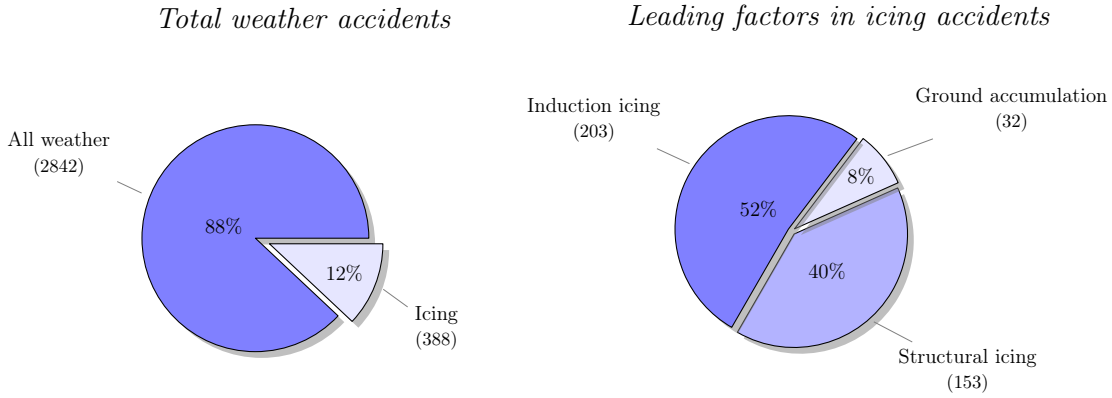

Figure 1.1: A statistical overview of icing accidents.
Data are collected from a sample of 3230 accidents occurred between the years 1990-2000. Data are taken from Ref. [1].

the performance degradation of the lifting surfaces and to help the design of the anti-icing prevention systems. These numerical analyses have also and important role in the reduction of the number of preliminary tests in wind tunnel and so in the reduction of the preliminary design costs. A very reliable software can substitute a certain number of expensive tests in wind tunnel: icing tests require special wind tunnels that can operate at low temperatures, so their costs are much more than usual aeronautical wind tunnels.

1.1 Fundamentals of ice accretion

In this section it is proposed a brief explanation of the physics of ice accretion and an overview of the different types of ice that can occur in aeronautical applications. The attention is mainly focused on the parameters governing the phenomenon and on the atmospheric conditions that can facilitate the appearance of the ice.

1.1.1 Parameters governing the ice accretion

Ice accretion happens when a plane flies through a cloud containing supercooled water. Water droplets in supercooled state are particular because they have a temperature at or below 273 K (0 °C) but they still remain liquid. When these droplets impact over a cold surface their unstable state of equilibrium is broken and they quickly freeze on it.

The rate at which the ice grows depends on different parameters. The most relevant ones are: the *Liquid Water Content* (LWC), the *collection efficiency* (and so the shape), the *droplet size* (MVD), the *airspeed*, the *surface roughness* and of course the *outside air temperature*.

Liquid Water Content (*LWC*)

The *Liquid Water Content* (LWC) represents the density of the supercooled liquid water contained in the cloud and it is expressed in grams of water per cubic meters of air [g/m^3]. The amount of water in the cloud straightly affects the ice accretion rate but not always high values of LWC correspond to high values of accretion rate. That's because if the temperature is not low enough, the collected water tends to accumulate and flow away before freezing completely.

Typical values of LWC are between 0.2 and 1.5 g/m^3 depending on the type of cloud (see tab. 1.1).

Cloud type	**LWC** [g/m^3]
Fog	0.06
Stratus	0.28 ÷ 0.3
Stratocumulus	0.44
Cirrus	0.06
Cumulus	0.25 ÷ 0.3
Cumulonimbus	1.00 ÷ 3.0
Stratus	0.30

Table 1.1: Typical values of LWC in different cloud types taken from Ref. [10].

Mean Volume Diameter (*MVD*)

The *Mean Volume Diameter* (MVD) is a statistical value representing the mean diameter of the droplets carried by the cloud (usually measured in μm). MVD is strongly dependant on the air temperature: small droplets are typical of low temperature clouds, instead large droplets appear in warmer clouds. As the temperature decreases, droplets have to reduce their radius to reduce their surface and minimize the heat exchange with the surrounding air. In atmosphere, water can stay in supercooled state until maximum 233 K (-40 °C).

The dimensions of the droplets affects foremost the impact limits and the way the surface collect the water from the cloud. Large droplets have a large mass and a large inertia, so they tend to follow a straight trajectory and not to follow the streamlines around the body. On the other hand small droplets are more sensitive to the irregular shapes of the body (horns, spikes, high curvatures in general).

Typical values of MVD are between 15 and 40 μm. Droplets with higher values are called *Supercooled Large Droplets* (SLD) and they are characteristic of the freezing rain. SLD is a very critical condition for flight because the resulting ice is highly spread along the surfaces affecting the whole pressure field and the ice accretion is very rapid (even if the outside air temperature is slightly below 0 °C). An example of this kind of ice accretion is shown in Fig. 1.2. The aforementioned incident of the American Eagle

Flight 4184 occurred in SLD conditions during a freezing rain because the ice suddenly froze the ailerons movements [15].

Figure 1.2: An example of the effects of the freezing rain over a wing. The ice covers the entire surface of the wing. Image taken from Ref. [2].

Collection efficiency (β)

The *collection efficiency* is one of the most important parameter in ice accretion because it is strictly related to the accretion rate. It represents the distribution of the water collected by the surface from the cloud and can be an index of how much surface will be affected by the ice accretion. It is defined as the ratio between the area far upstream and the area on the surface enclosed by the same droplet impact trajectories. It is a local value and, according to Fig.1.3, on a three-dimensional geometry it can be expressed as:

$$\beta = \frac{\mathrm{d}A_\infty}{\mathrm{d}A_i} \tag{1.1}$$

Typical values of the collection efficiency are between 0 (clean surface) and 0.8 (stagnation points) where high values of β are related to high values of the ice-accretion rate. The collection efficiency is heavily affected by several parameter like the chord length, the airspeed, the MVD and the air temperature. For example, airfoils with small leading edge radius or high values of MVD are related to high value of the collection efficiency. An overview of these behaviours can be seen in Fig. 1.4.

Airspeed (V)

Airspeed affects many aspects of the ice-accretion process. First of all it is involved in the droplet collection, high velocities let the surface intercept more air and so a potential

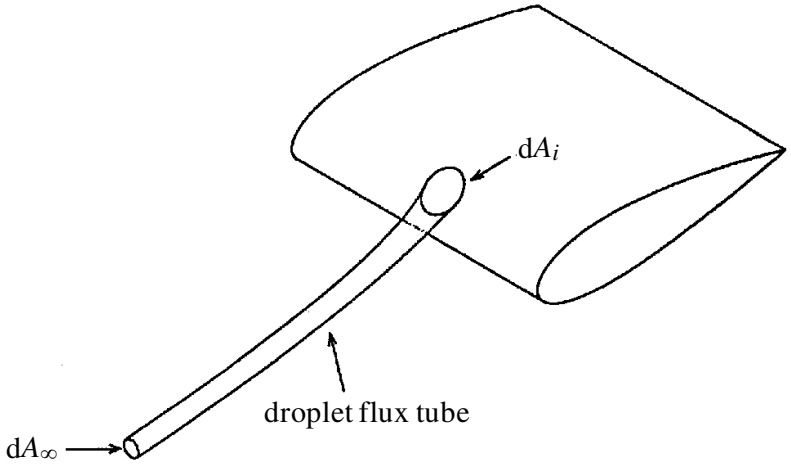

Figure 1.3: Definition of the local collection efficiency over a three-dimensional surface. Figure taken from Ref. [3].

greater mass of water. This may increases the ice accretion rate. On the other side, the airspeed is also responsible of an aerodynamic heating term due to friction effects and of the wall shear stress that drive away the surface water.

Air temperature and Surface temperature

Icing process is controlled by the heat exchanges between the impinging supercooled droplets, the ice already developed, the aircraft surface and the atmosphere. The *outside air temperature* governs the amount of the heat exchanged between the water layer and the outside atmosphere: the lower the outside temperature, the higher the heat exchange ratio and the fastest the ice accretion process. Air temperature influences also the droplet size (MVD), clouds with lower temperature contain droplets with smaller radius.

The control of the *surface temperature* is one of the most used methods to prevent or delay the ice accretion. It is important to note that the process is however governed by the heat fluxes so, if the heat flux imposed at the surface is not sufficient to balance the heat lost by convection and evaporation on the superficial water, the surface temperature can be lead to the freezing point and the icing process can occur anyway.

Surface roughness (k)

The *surface roughness* (k) is a very difficult parameter to be measured. It is usually expressed in term of equivalent sand grain roughness (μm) and it is a very sensitive parameter in the computation of the convective heat transfer coefficient (h_c). Its value fixes the transition point between the laminar and the turbulent boundary layer and so it sets a different law for the h_c calculation on different portion of the surface. A turbulent boundary layer has generally a greater values of the h_c because of its higher grade of

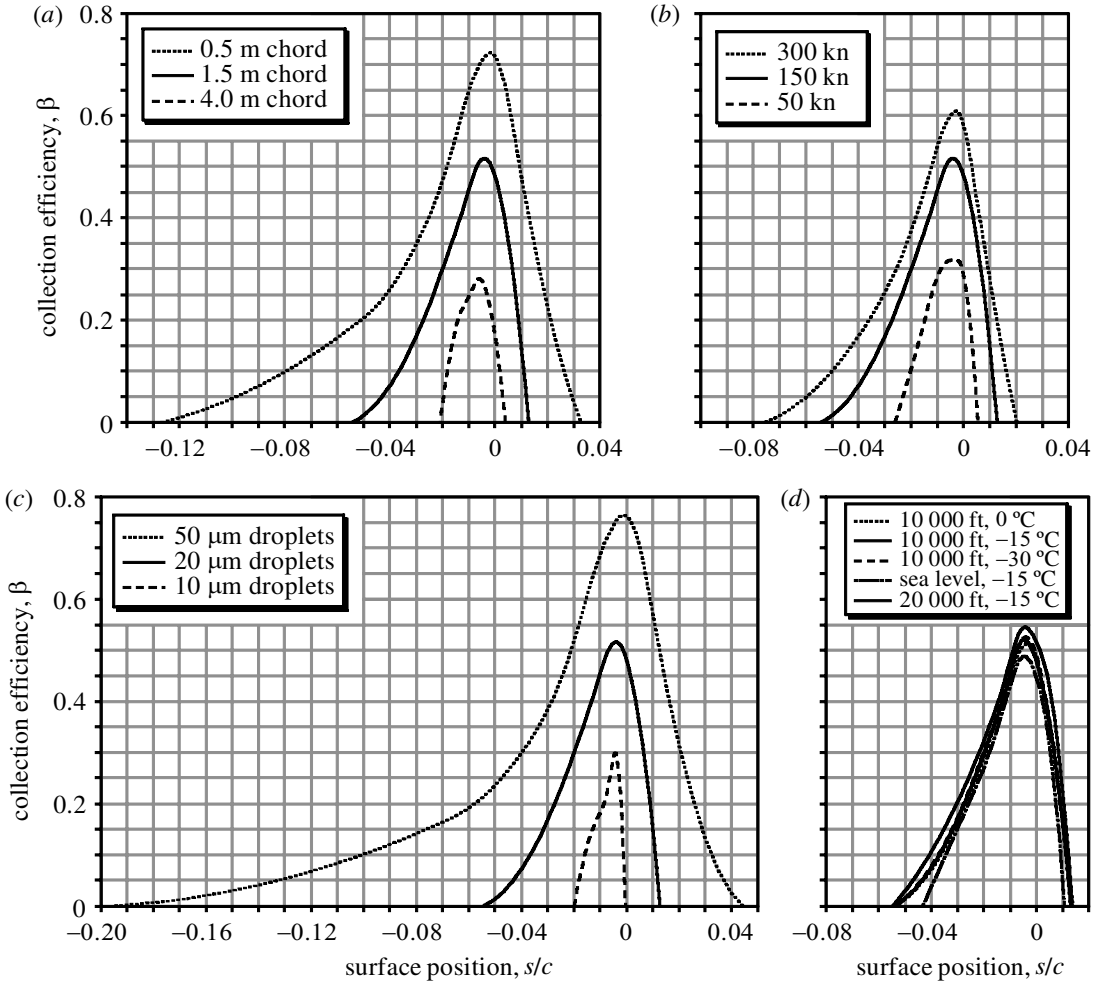

Figure 1.4: Effects of the key parameters on the collection efficiency: (a) Airfoil chord, (b) Airspeed, (c) MVD, (d) Altitude (outside air temperature). Figure taken from Ref. [3].

internal mixing. A more complete analysis of icing roughness modelling can be found in [19].

1.1.2 Types of aeronautical ice accretions

Ice accretion process can lead to different kinds of ice formations with different ice proprieties and behaviours depending on the external weather conditions. The three main categories of aeronautical ice accretion are: *rime* ice, *glaze* (or clear) ice and *mixed* ice. At the end of the section, the weather conditions for these different types of ice accretion are summarized in Tab. 1.2.

Ice accretion process is generally subdivided in two phases: a first period of rime-ice

accretion followed by the glaze-ice accretion [11]. The duration of the rime and glaze phases depends on the weather conditions, for example at temperatures near the 273 K (0 °C) the glaze phase appears almost immediately, otherwise in very cold situations the rime phase lasts for long time.

Rime ice

Rime ice is the ice accretion with the milky opaque aspect (see Fig. 1.5). It forms in conditions of low temperature (below 263 K, -10 °C), low LWC values, small MVD, and low velocities. It is the result of a very rapid (almost instantaneous) freezing of the collected water which traps inside some bubbles of air. These bubbles give the rime ice its typical opaque aspect.
Rime ice is generally very rough and porous due to the air bubbles and forms accretions with smooth shapes interesting the leading edge of the wings. Its density is lower than the glaze ice (around 880 g/m^3 for rime ice against 920 g/m^3 for glaze ice) and it is easier to be removed by the de-icing systems due to its friability.

Figure 1.5: An example of rime-ice accretion. Image taken from Ref. [4].

Glaze ice

Glaze ice, also called clear ice, is the ice accretion with the clear and translucent aspect (see Fig. 1.6). It forms at high velocities, warmer temperatures (near 273 K, 0 °C) and in clouds with high values of LWC. In glaze-ice accretion process the surface is always covered by a thin film of unfrozen water that is driven back by the wall shear stresses before completely freeze. This aft solidification lead to the formation of horns in the vicinity of the leading edge that can protrude widely toward the direction of motion. Glaze ice is denser and harder than the rime ice and it is more difficult to be broken by the de-icing systems. In this category can be included also the freezing rain.

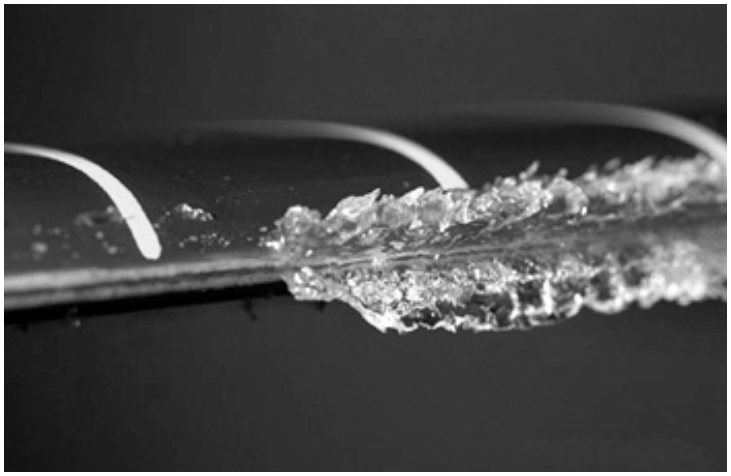

Figure 1.6: An example of glaze-ice accretion. Image taken from Ref. [5].

Mixed ice

Mixed ice is the transitional state between the rime and the glaze ice. It forms at temperature between 258 K and 265 K and has intermediate characteristics between the rime and the glaze ice.

Ice type	**Air Temp.** $[K]$	**LWC**	**MVD**	**Velocity**
Rime	< 263	low	low	low
Mixed	$258 \div 265$	medium	medium	medium
Clear	$263 \div 273$	high	high	high

Table 1.2: Summary of the whether conditions and the related common ice accretion typologies.

1.2 In-flight icing risks and protection systems

Icing effects over an aircraft may be very different; they can affect the performances, reduce the functionalities of the on-board systems and preclude the safety.
Regarding the loss of the aerodynamic performance many studies showed a reduction of the maximum lift and an incredible increase in the drag (i.e. see Fig. 1.7). The unexpected reduction of the maximum lifting coefficient is reflected by an increase of the stall speed which in some situations, like during the landing phase, can be very hazardous. For example, as reported by an AGARD report of the 1997, a 35% loss in maximum lift is related to a 24% increase of the stall speed (see Fig. 1.7 from [3]). On the other side the increase of the drag affects significantly the efficiency of the wing

and of the entire aircraft: it is not unusual that the drag coefficient increases more than the 200% [3]. Beyond the economical effects, these aerodynamic limitations affects also the manoeuvrability of the plane, for example the performance degradation of the tail surfaces can modify the pitch response of the aircraft.

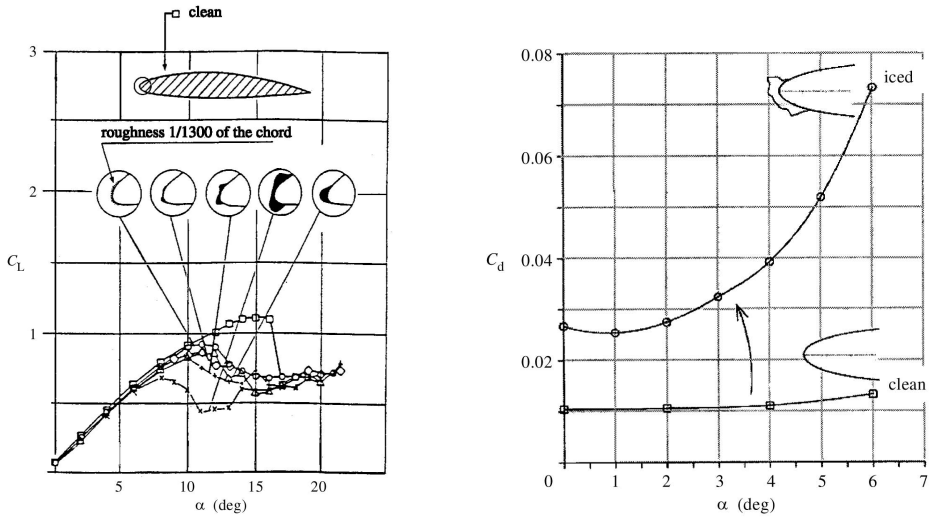

(a) C_L degradation (b) C_D degradation

Figure 1.7: Aerodynamic performance degradation due to ice accretion. Figures taken from Ref. [3].

Other problems caused by icing regard the blockage of the moving surfaces, like the ailerons, the obstruction of the engine intake or the carburetor inlets, and the occlusion of the aircraft probes, such as for example the Pitot tube. In all these cases in-flight safety can be compromised.
For aircraft with piston-engines the ice accretion in the carburetor lead to a reduction of the intake air and a consequent drop in the engine power. To avoid this problem, there are specific charts showing the critical atmospheric conditions for the carburetor in use. In the same way, for turbojet and turbofan engines, ice formation over the intake reduces the amount of the captured air and the detachment of the ice accreted over the initial stages of the compressor may possibly lead to the damage of some rotor or stator blades. Regarding the probes, the Pitot tube is particularly vulnerable because of its very small curvature radius and small pressure taps; its obstruction may alter the measure of the flight speed.

In order to delay or prevent ice formation or to remove the accreted ice, different systems and methods have been developed. The two main categories of ice protection systems are the *de-icing* systems and the *anti-icing* systems:

De-icing systems are activated during the flight and are used to break the ice already accreted. To this category belong for example pneumatic systems that break the ice deforming specific parts of the surface (i.e. the leading edge). These deformable parts are usually made by strong rubber. An example of a pneumatic anti-icing system is shown in Fig. 1.8.

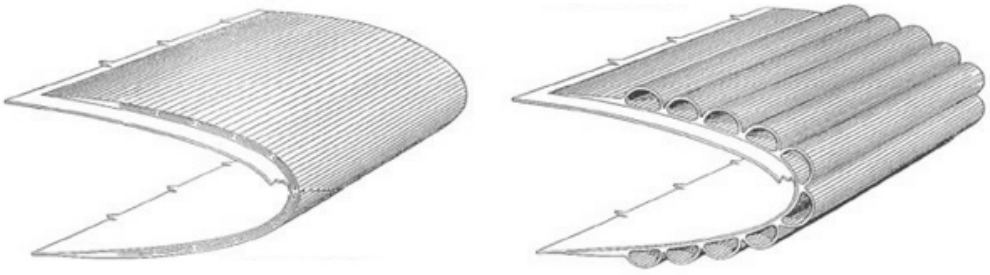

Figure 1.8: Example of a pneumatic de-icing system.
Images taken from Ref. [1].

Anti-icing systems concern the prevention and the delay of the ice formation. To this category belong systems that heat-up the surface of the wing and chemicals or foams that delay the ice accretion. Foams and chemicals are applied on ground before the flight over the surfaces to protect. These substances, like the glycol, are usually sprayed and have the function to lower the freezing point of water or to create a layer on which the ice slip away. On the other hand, the heating systems are activated during the flight and their activation may lead to the formation of the so-called "runback-ice"; a kind of ice derived from the melted ice that flows away and re-freezes afterwards. For this reason it is very important to determine the right moment to activate the protection systems. An example of the application of the chemicals is shown in Fig. 1.9.

An extensive overview of anti-icing and de-icing systems can be found in reference [20].

1.3 Icing Models

Starting from the fundamental formulations proposed by F. Neumann, B.P. Clapeyron and G. Lamé, among others, J. Stefan in 1889 gave the first mathematical description of the liquid water-ice two-phase problem, in connection with ice formation in the polar sea [21]. Moving from these early works, the so-called Stefan problem was then generalized to describe many different physical systems where phase change can possibly occur, such as for example chemical processes and melting/solidification in industrial metal processes.

The two most used aeronautical icing models have been developed by Messinger in 1953 [7] and by Myers in 2001 [11]. Messinger's model was the first aeronautical icing model and it is based on an equation enforcing the equilibrium of the heat fluxes at the surface, whereas Myers presented an extension of the Messinger model based on a

Figure 1.9: Example of the application of the anti-icing chemicals. Image taken from Ref. [6].

simplified formulation of the Stefan problem. The model formulated by Myers introduce a more accurate description of the transition from rime to glaze-ice regime and, differently from the Messinger model, in which the substrate is assumed to be isolated, Myers added a description of the heat diffusion problem through the ice and the water layers in order to account for the heat transfer at the aircraft surface [11]. During the last years these two icing models have been slightly modified and improved with the introduction of a more accurate description of the liquid film behaviour [22], [23], more accurate methods for the computation of the convective heat transfer [19], and a more suitable treatment of the run-back ice [19], [24]. Nowadays these models remains the basis of the icing prediction codes.

1.4 Numerical and experimental researches

From the 1960s, with the rapid improvements in computer development, the numerical simulation became more and more influential in aircraft design. The first computers could only afford to solve potential flow simulation, but nowadays a desktop computer can solve the full Navier-Stokes equations in a reasonable amount of time. During the last years, several CFD (*Computational Fluid Dynamic*) codes have been developed to simulate more and more accurately the real behaviour of fluids and the CFD has become a fundamental tool in aerodynamic research.

In icing studies, numerical simulations are very important in the preliminary design of the lifting surfaces and anti-icing systems. In this way it is possible to reduce the number, and so the costs, of the preliminary tests in wind tunnel. They can provide a preliminary idea of the performance degradation, they can be used to obtain the most

critical ice shape that can occur during a flight of the plane and they can facilitate the design of the anti-icing systems.

1.5 Goals and structure of the thesis

The aim of the present work is to develop a new icing model based on the unsteady exact solution of the Stefan problem in the glaze ice regime. The present manuscript is organised as follows.

In Ch. 1 the physical description of the problem was introduced, the most important parameters governing the ice accretion were presented and the different types of ice that can occur in aeronautical applications were analysed.

In Ch. 2 the quasi-steady models describing the icing problem are presented. The attention is mainly focused on the hypothesis used to develop these models. In § 2.1 the first model developed by Messinger is briefly described, then in the following sections the models based on the Stefan problem are presented. The Stefan problem concern the phase-change problems and it is the base of the Myers model ad its modified version shown in § 2.2.2 and §. 2.2.3.

In Ch. 3 the novel unsteady icing model is presented. The quasi-steady hypothesis is relaxed in the glaze-ice regime and the exact solution of the Stefan problem is deduced using a similarity approach. In § 3.3 some comparisons between the quasi-steady and the unsteady model are discussed.

In Ch. 4 the importance of the use of the local temperature near the body instead of the upstream static temperature is discussed with some comparisons.

In Ch. 5 the icing code PoliMIce is briefly introduced and the new model is applied in different atmospheric conditions in order to show the behaviour of the new improvements introduced in Ch. 3 and Ch. 4.

Chapter 2

Quasi-steady ice accretion models

In this chapter the state of the art of icing models is presented. The attention is mainly focused on their approximation hypothesis and inconsistencies in order to lay the foundations for Ch. 3.

In § 2.1 the first icing model proposed by Messinger (1953) is discussed, while in §. 2.2 the most recent model proposed by Myers (2001) and later modified by Gori (2013) are presented. These two models are both based on the approximate solution of the Stefan problem whereas the Messinger's consists only in a heat balance at the surface. Before that, in § 2.2.1, the Stefan problem is briefly recalled.

2.1 Messinger model

Messinger model has been developed in 1953 by Bernard Messinger and exposed in his paper *"Equilibrium Temperature of an UnHeated Icing Surface as a Function of Air Speed"* [7]. In this work Messinger proposed an analysis of the equilibrium temperature reached by an unheated surface in several icing conditions and with different values of the parameters presented in § 1.1.1.

Messinger's model is based on the energy balance between the water (or ice) layer and the atmosphere surrounding the surface. The thermal fluxes involved in the process are: the heat lost by *convection*, the heat lost by *sublimation* or *evaporation*, the heat lost due to the *warming of the impinging water*, the heat gained from the *release of the latent heat of fusion*, the heat gained from the *viscous effects* and the heat gained from the *kinetic energy* of the impact of the droplets. These contributions are shown in Fig. 2.1, are summarized in Tab. 2.1 and they will be extensively discussed in § 2.2.2.

The model is based on two main hypothesis:

- The temperature within the water and the ice layer is assumed to be constant and equal to the equilibrium temperature.
- The substrate is insulated.

A new idea in this model is the introduction of the *freezing fraction*, a quantity defined as the mass of ice divided by the mass of the incoming fluid.

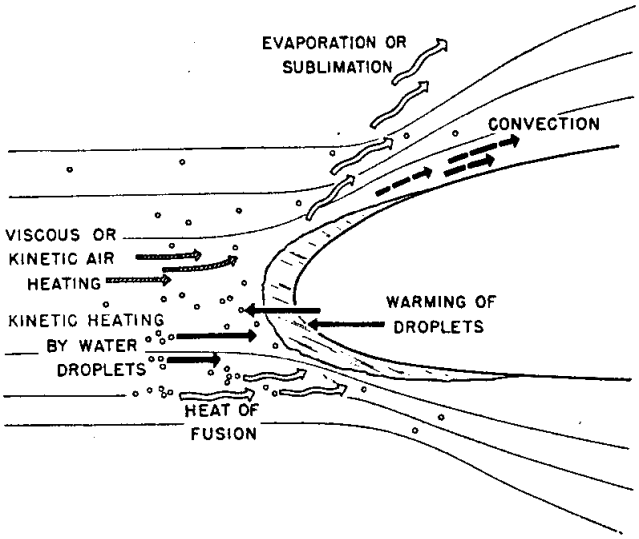

Figure 2.1: Scheme of the heat exchange terms involved in Messinger model. Figure taken from Ref. [7].

A problem of the Messinger model is the assumption of the isothermal ice layer, this lead to a freezing fraction that changes instantaneously from zero to one without transition. According to the Stefan studies [[21]], the freezing fraction is a continuous function that decreases monotonically. Another limitation of the model is that it doesn't take into account the thermal conduction through the substrate due to its insulation. As a result of these limitations, the total ice accretion is under-estimated respect to the experimental results.

Heat sources	
Convection	$(\dot{q}_c)$
Sublimation or Evaporation	$(\dot{q}_s, \dot{q}_e)$
Warming of the impinging water	$(\dot{q}_w)$
Release of the latent heat of fusion	$(\dot{q}_l)$
Viscous effects	$(\dot{q}_v)$
Kinetic energy	$(\dot{q}_k)$

Table 2.1: Thermal fluxes involved in the Messinger model: heat *loss* are written in red whereas heat *gained* in green.

2.2 Models based on the Stefan problem

The first theoretical work on phase-change problems have been proposed by G. Lamé and E. Clapeyron in their 1831 paper *"Mémoire sur la solidification par refroidissement d'un globe liquide"* [25]. In this work the two authors were interested in the investigation of water solidification due to liquid cooling. Few years later, in 1889, the mathematician Joseph Stefan during his studies in ice formation in polar sea, proposed the first complete mathematical model describing the ice accretion phenomenon [21]. This model is still used in many problems such as the metal melting in industrial processes or the ice formation from water cooling, and in the early years it has been improved to taking into account multiphase processes (see for example Ref. [26]).

2.2.1 The Stefan problem

The Stefan problem is a set of four Partial Differential Equations (PDEs) describing the evolution of a single-component two-phase system during a phase change. Its complete solution gives the temperature distribution within the solid and the liquid layers and the position of the interface at each time. This kind of problem belongs to the family of the so-called *moving-boundary problems* because the position of the solid-liquid interface is unknown and depends on the time and on the solution itself.

Considering the reference system in Fig. 2.2, the one-dimensional Stefan problem reads

$$\begin{cases} \dfrac{\partial T}{\partial t} = \dfrac{K_s}{\rho_s C_s}\dfrac{\partial^2 T}{\partial z^2} \\ \dfrac{\partial \vartheta}{\partial t} = \dfrac{K_l}{\rho_l C_l}\dfrac{\partial^2 \vartheta}{\partial z^2} \\ \rho_s \dfrac{\partial B}{\partial t} + \rho_l \dfrac{\partial h}{\partial t} = \dot{m}_{\text{in}} - \dot{m}_{\text{out}} \\ \rho_s L_F \dfrac{\partial B}{\partial t} = K_s \left.\dfrac{\partial T}{\partial z}\right|_{B(t)^-} - K_l \left.\dfrac{\partial \vartheta}{\partial z}\right|_{B(t)^+} \end{cases} \tag{2.1}$$

where the subscripted index s and l stands for the *solid* and the *liquid* phase and the z coordinate is aligned along the normal of the surface. Typical values for the parameters entering in equations 2.1 are reported in Tab. 2.2.

The first and the second equations of 2.1 describe the heat diffusion within the solid and the liquid phase respectively. The third equation is the continuity equation and enforces the mass conservation law. The source term in this equation may be for example the mass lost by the evaporation and the mass gained from an external source. The fourth equation is the so-called Stefan condition and it is an energy balance relating all the heat fluxes involved in the phase change at the solid-liquid interface. It guarantees that the latent heat due to the phase change is equal to the net flux of heat from and towards the upper ($\dot{Q}^{\uparrow}_{\text{up}}$) and the lower ($\dot{Q}^{\downarrow}_{\text{down}}$) layers. In other words it can be interpreted as the

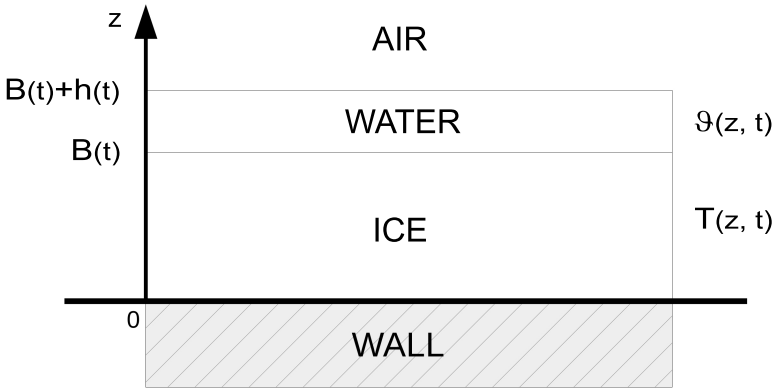

Figure 2.2: Reference system for a mono-dimensional two-phases Stefan problem.

velocity of the moving boundary produced by the difference between the heat fluxes at the interface.
In Fig. 2.3 a visual representation of $\dot{Q}^{\uparrow}_{\text{up}}$ and $\dot{Q}^{\downarrow}_{\text{down}}$ is given in order to help the comprehension of the next sections.

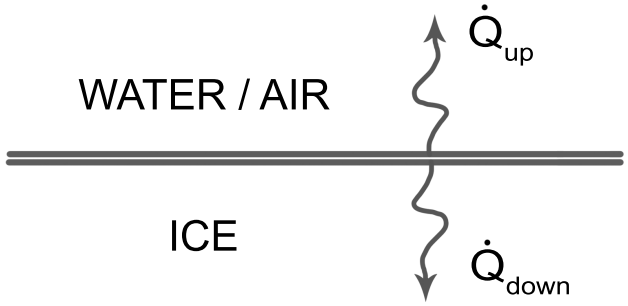

Figure 2.3: Representation of the $\dot{Q}^{\uparrow}_{up}$ and $\dot{Q}^{\downarrow}_{down}$.

The two icing models that will be presented in the next two sections both introduce a number of assumptions leading to a simplified formulation of the complete problem. In particular the problem is transformed to a set of Ordinary Differential Equations (ODEs) instead of PDEs. Solving this simpler system allows to obtain a closed-form solutions and to develop procedures which are adequately simple to be implemented in icing prediction codes.

2.2.2 Myers model

Myers model has been developed by Tim G. Myers in 2001 [11] as an extension of the original Messinger model described in § 2.1. In its work Myers proposed a simplified solution of the one-dimensional Stefan problem in order to take into account the conduction of the heat in the ice layer. With the introduction of some simplification, the temperature

profile within the ice layer can be calculated instead of assuming to be a constant function like in Messinger [7]. In this way also the freezing fraction assumes a more suitable shape.

First of all it is now recalled for ease the Stefan problem shown in Eq. 2.1 with some adaptations for aeronautical purpose:

$$\begin{cases} \dfrac{\partial T}{\partial t} = \dfrac{K_i}{\rho_i C_i} \dfrac{\partial^2 T}{\partial z^2} \\ \dfrac{\partial \vartheta}{\partial t} = \dfrac{K_w}{\rho_w C_w} \dfrac{\partial^2 \vartheta}{\partial z^2} \\ \rho_i \dfrac{\partial B}{\partial t} + \rho_w \dfrac{\partial h}{\partial t} = \beta \, \mathrm{LWC} \, V_\infty \\ \rho_i L_F \dfrac{\partial B}{\partial t} = K_i \left. \dfrac{\partial T}{\partial z} \right|_{B(t)^-} - K_w \left. \dfrac{\partial \vartheta}{\partial z} \right|_{B(t)^+} \end{cases} \tag{2.2}$$

The subscripted indexes are become i for the *ice* phase and w for the *water* phase and the source term in the mass conservation law has been adapted using the parameters of Ch. 1.1. Therefore the source term is $\beta \, \mathrm{LWC} \, V_\infty$ and it represents the amount of water collected every second from the atmosphere by the surface. Indeed, once multiplied by the surface, this term has the dimensions of $[kg/s]$.

The hypotheses introduced by Myers are now summarized:

- The physical properties of ice and water do not depend on the temperature
- The phase change from water to ice occurs at a fixed temperature assumes to be the freezing temperature (273 K).
- The substrate (i.e. the wall) is maintained at a constant temperature, usually assumed to be equal to the air temperature. This assumption is justified by the great dimensions of the body and the high value of the thermal conductivity of its material (usually aluminium).
- Droplets are in thermal equilibrium with the surrounding air, so their temperature is supposed to be equal to the air temperature.
- The time scale governing the heat diffusion problem is larger than the ice accretion time scale. This hypothesis will be verified later.
- The water layer (if present) is infinitesimal, therefore its internal temperature can be considered approximately constant.

In his formulation, Myers derived two different accretion laws for the rime-ice and the glaze-ice, defining a criterion based on the so-called *rime limit thickness* (B_g) in order to discern whether rime or glaze ice occurs. In the following sections these two accretion

models, are presented but firstly it is necessary to introduce the heat fluxes involved in the process.

Heat fluxes

The heat fluxes involved in the process are now briefly explained.

$\dot{\mathbf{Q}}_\mathbf{c}$: is the *convective* heat flux exchanged between the ice ($\dot{Q}_{ci}$) or the water ($\dot{Q}_{cw}$) layer and the surrounding air.

$$\dot{Q}_{c\star} = h_{c\star}(T - T_\infty)\, A \tag{2.3}$$

where $h_{c\star}$ is the convective heat transfer coefficient and the $\star$ symbol is a placeholder standing for $i$ce or $w$ater.

$\dot{\mathbf{Q}}_\mathbf{e}$ and $\dot{\mathbf{Q}}_\mathbf{s}$: are respectively, the evaporation and the sublimation heat fluxes exchanged between the ice ($\dot{Q}_s$) or the water ($\dot{Q}_e$) layer and the surrounding air. Both of these heat fluxes have the same form:

$$\dot{Q}_{e,s} = \chi_{e,s}\left[e_{(T)} - e_{(T_\infty)}\right]\, A \tag{2.4}$$

χ is the evaporation (or sublimation) coefficient and $e(T)$ is the evaporation (or sublimation) function. The $e_{(T)}$ function returns the vapour pressure from the temperature and in a certain region near the 273 K (0 °C) it can be approximated as a linear function, so

$$\dot{Q}_{e,s} = \chi_{e,s}\; e_0\,(T - T_\infty)\; A \tag{2.5}$$

For further informations see [11].

$\dot{\mathbf{Q}}_\mathbf{d}$: is the term that take into account the *cooling* provided *by the incoming droplets*. This heat flux exists because the droplets that impact on the surface release their latent heat and it is present in the energy balance only when the droplets have a temperature different from the upstream static temperature. The $\dot{Q}_d$ reads:

$$\dot{Q}_d = \beta\, \mathrm{LWC}\, V_\infty C_w (T - T_d)\, A \tag{2.6}$$

where T_d is the droplet temperature. In many cases this term is considered to be zero because T and T_d are supposed to be equal.

$\dot{\mathbf{Q}}_\mathbf{k}$: is the heat flux associated to the *kinetic energy* of the impacting droplets.

$$\dot{Q}_k = \frac{1}{2}\left(\beta\, \mathrm{LWC}\, V_\infty A\right) V_\infty^2 \tag{2.7}$$

$\dot{\mathbf{Q}}_\mathbf{l}$: is the heat flux associated to the release of the *latent heat* of fusion or solidification.

$$\dot{Q}_l = \rho_i L_F \frac{\partial B}{\partial t}\, A \tag{2.8}$$

where L_F is the latent heat of fusion of the water. Its value is reported in Tab. 2.2.

$\dot{\mathbf{Q}}_\mathbf{a}$: is the heat flux associated to the *aerodynamic heating*. It is produced by the friction of the air over the surface.

$$\dot{Q}_a = \frac{1}{2} \frac{R_c \, h_c \, V_\infty^2}{C_{p_{air}}} A \tag{2.9}$$

where h_c is the convective heat transfer coefficient, R_c is the adiabatic recovery factor to take into account the compressibility of the air and $C_{p_{air}}$ is the specific heat of the air evaluated at constant pressure.

$\dot{\mathbf{Q}}_\mathbf{irr}$: is the radiative heat flux but it is usually neglected.

$$\dot{Q}_{irr} = \sigma \left(T^4 - T_\infty^4 \right) A \tag{2.10}$$

Parameters			**Value**
Density	$[Kg/m^3]$	$\rho_{i_{glaze}}$	917
		$\rho_{i_{rime}}$	800
		ρ_w	1000
Latent heat	$[J/Kg]$	L_S	$2.83 \cdot 10^3$
		L_F	$3.344 \cdot 10^5$
		L_E	$2.26 \cdot 10^6$
Specific heat	$[J/KgK]$	$C_{p_{air}}$	1014
		C_i	2050
		C_w	4218
Evaporation coeff.	$[m/s]$	χ_e	11.0
Sublimation coeff.	$[m/s]$	χ_s	$13.77 \cdot 10^{-3}$
Vapour pressure	$[Pa/K]$	e_0	27.03
Convective coeff	$[W/m^2K]$	h_{is}	1000
		h_{aw}	500
Thermal conductivity	$[W/mK]$	K_w	0.571
		K_i	2.18

Table 2.2: Typical values of the parameters used to calculate the heat fluxes taken from Ref. [11].

Rime-ice problem

As seen in Ch. 1.1, rime-ice accretion occurs with very low temperatures, low values of the MVD and low velocities. In these conditions the collected water freezes almost instantaneously and so the accretion scheme is only composed by the surrounding air, the ice layer and the wall (Fig. 2.4).

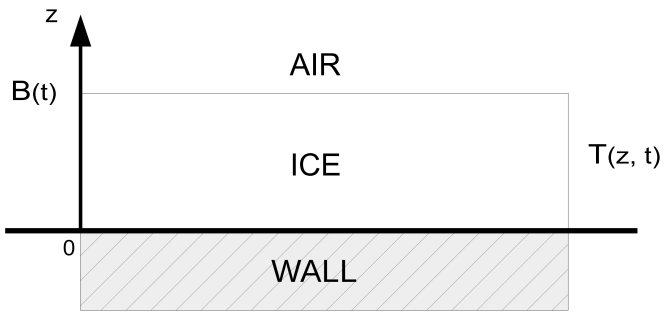

Figure 2.4: Reference system for the rime-ice problem.

The boundary conditions for the rime-ice accretion are:

$$\begin{cases} T_{(0,t)} = T_{\text{wall}} \\ -K_i \left.\dfrac{\partial T}{\partial z}\right|_B = \left(\dot{Q}_{ci} + \dot{Q}_s + \dot{Q}_d\right) - \left(\dot{Q}_{ai} + \dot{Q}_k + \dot{Q}_l\right) \triangleq \dot{Q}^{\uparrow}_{\text{up}} \end{cases} \tag{2.11}$$

where the term $\dot{Q}^{\uparrow}_{\text{up}}$ represents the total net amount of heat exchanged by the ice surface with the external airflow.

The hypothesis that the ice growth rate is significantly slower than the heat conduction rate through the ice layer leads to a substantial simplification of the equation system. The Fourier equation in the ice (Eq. 2.1.a) becomes a quasi-steady ODE, so

$$\frac{\partial^2 T}{\partial z^2} \approx 0 \tag{2.12}$$

However, this simplification can be applied only under certain conditions. According to Myers [11], the non-dimensional typical height of the ice layer is

$$\hat{B} \approx \frac{K_i}{(1-\phi)\beta\,\text{LWC}\,V_\infty C_{P_i}} \tag{2.13}$$

where ϕ is the fraction of water that remains liquid. In rime ice this value is zero because the whole water freezes instantaneously. Using the coefficient values in Tab. 2.2 and the reference values of the icing parameters in Tab. 2.3, the Eq. 2.13 gives a typical ice thickness of $\hat{B} \sim 2.4$ cm.

Parameter	Value
ϕ	0
β	0.55
LWC	0.001 g/m^3
V_∞	90 m/s

Table 2.3: Reference parameter used in Eq. 2.13.

So, the aforementioned simplification can be applied until $B \ll 2.4$ cm.

Under this condition the heat diffusion equation can be approximated to the leading-order quasi-steady problem. The temperature profile within the ice layer can be retrieved by integrating twice Eq. 2.12 with the proper boundary conditions 2.11. This leads to a linear temperature profile within the ice layer which results in the following expression:

$$T_{(z)} = T_{\text{wall}} + \frac{\dot{Q}_{ai} + \dot{Q}_k + \dot{Q}_l - \left(\dot{Q}_{ci} + \dot{Q}_d + \dot{Q}_s\right)}{A\left(K_i + \dfrac{B}{A\left(T_{\text{wall}} - T_\infty\right)}\left(\dot{Q}_{ci} + \dot{Q}_d + \dot{Q}_s\right)\right)} z \tag{2.14}$$

It can be further simplified in

$$T_{(z)} \approx T_{\text{wall}} + \frac{\dot{Q}_{ai} + \dot{Q}_k + \dot{Q}_l - \left(\dot{Q}_{ci} + \dot{Q}_d + \dot{Q}_s\right)}{AK_i} z \tag{2.15}$$

because the second term at the denominator is usually very much smaller than K_i.

The accretion rate in the rime-ice condition can be immediately derived from the mass conservation law (Eq. 2.1.d) because the water height $h_{(t)}$ is null and so also its first derivative is zero. Therefore

$$\frac{\partial B}{\partial t} = \frac{\beta\,\text{LWC}\,V_\infty}{\rho_i} \tag{2.16}$$

The ice thickness $B_{(t)}$ is obtained by the integration of Eq. 2.16 with the initial condition $B_{(x,0)} = 0$. This leads to:

$$B_{(t)} = \int_0^t \frac{\beta\,\text{LWC}\,V_\infty}{\rho_i}\,dt = \frac{\beta\,\text{LWC}\,V_\infty}{\rho_i}\,t \tag{2.17}$$

In rime-ice condition it can be observed that the accretion rate $\partial B/\partial t$ is constant in time and so the ice thickness $B_{(t)}$ is a linear function of time.

Glaze-ice problem

Glaze-ice accretion occurs when the entire amount of the collected water does not freezes and a certain quantity flows along the surface or the underlying ice. In this condition the surface is always covered by a thin film of unfrozen water and the reference system is the one in Fig. 2.5.

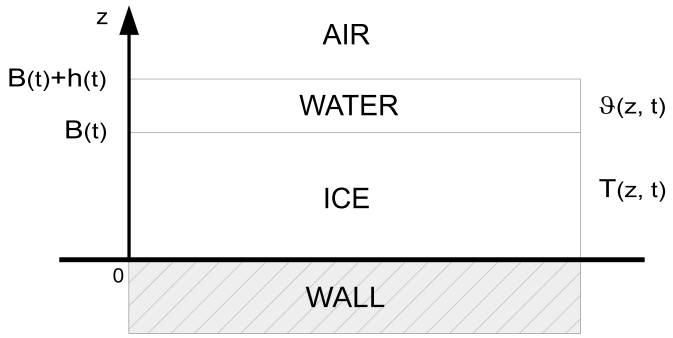

Figure 2.5: Reference system for the glaze-ice problem.

The boundary conditions have to be split in two part. In the water layer they are:

$$\begin{cases} T_{(0,t)} = T_{\text{freezing}} \\ -K_i \left.\dfrac{\partial T}{\partial z}\right|_B = \left(\dot{Q}_{ci} + \dot{Q}_e + \dot{Q}_d\right) - \left(\dot{Q}_{ai} + \dot{Q}_k\right) \triangleq \dot{Q}^{\uparrow}_{\text{up}} \end{cases} \tag{2.18}$$

while in the ice layer they are two Dirichlet conditions:

$$\begin{cases} T_{(0,t)} = T_{\text{wall}}, \\ T_{(B,t)} = T_{\text{freezing}}. \end{cases} \tag{2.19}$$

The second equation is justified by the hypothesis that the phase transition occurs at constant temperature equal to the freezing temperature T_{freezing}.

The time scale separation argument addressed in the previous section can be also applied in the glaze-ice regime in the water layer. In a non-dimensional form and using the same parameters of the previous section (Tab. 2.2 and Tab. 2.3), the typical maximum water height can be expressed as follows:

$$\hat{h} \approx \frac{K_w}{\phi\, \beta\, \text{LWC}\, V_\infty C_w} \sim 0.003\, m \tag{2.20}$$

The only parameter that changes respect Eq. 2.13 is the value of ϕ. Indeed, in the water layer $\phi > 0$ and the maximum height is reached when the entire water remain liquid, so

when $\phi = 1$. In aeronautical applications the typical height of the liquid film is of the order of $1/10\,mm$, so the condition $h \ll 3\,mm$ is verified almost everywhere on the surface and the heat equation in the water layer can be simplified in the quasi-steady ODE

$$\frac{\partial^2 \vartheta}{\partial z^2} \approx 0. \tag{2.21}$$

Integrating twice Eq. 2.21 the resulting function $\vartheta_{(z)}$ is a linear function in z and observing that the leading order term at the denominator is K_w, it can be further simplified

$$\begin{aligned} \vartheta_{(z)} = T_{\text{freezing}} + \frac{\dot{Q}_{ai} + \dot{Q}_k - \left(\dot{Q}_{ci} + \dot{Q}_d + \dot{Q}_e\right)}{A\left(K_w + \dfrac{h}{A\left(T_{\text{surface}} - T_\infty\right)}\left(\dot{Q}_{ci} + \dot{Q}_d + \dot{Q}_e\right)\right)}(z - B) \approx \\ \approx T_{\text{freezing}} + \frac{\dot{Q}_{ai} + \dot{Q}_k - \left(\dot{Q}_{ci} + \dot{Q}_d + \dot{Q}_e\right)}{AK_w}(z - B) \end{aligned} \tag{2.22}$$

Even if this function is formally linear in z, the temperature can be considered constant and equal to the freezing temperature because of the very small variation across the ice layer due to the very thin water height assumption.

$$\vartheta_{(z)} \approx T_{\text{freezing}} \tag{2.23}$$

However the exact form of Eq. 2.22 is important in the evaluation of the $\partial\vartheta/\partial z$ derivative in the Stefan condition (Eq. 2.1.d). An important consequence of the isothermal hypothesis in the water layer is that the heat fluxes can be calculated using T_{freezing} instead of the unknown temperature at the free water surface T_{surface}.

In the ice layer the simplification to the quasi-steady ODE is still valid, so

$$\frac{\partial^2 T}{\partial z^2} \approx 0 \tag{2.24}$$

can be integrated twice with the boundary conditions Eq. 2.19 to obtain the temperature profile $T_{(z)}$:

$$T_{(z)} = T_{\text{wall}} + \frac{T_{\text{freezing}} - T_{\text{wall}}}{B} z \tag{2.25}$$

In order to obtain the glaze-ice accretion rate it is necessary to use the Stefan condition here recalled

$$\rho L_F \frac{\partial B}{\partial t} = -K_w \frac{\partial \vartheta}{\partial z}\bigg|_{B(t)^+} + K_i \frac{\partial T}{\partial z}\bigg|_{B(t)^-}. \tag{2.26}$$

Once derived Eq. 2.15 and Eq. 2.22 and substituted in the Stefan condition, the accretion rate is deduced to be:

$$\begin{aligned} \frac{\partial B}{\partial t} &= \frac{1}{\rho_{i_{\text{glaze}}} L_f}\left(\frac{\dot{Q}_{ci} + \dot{Q}_d + \dot{Q}_e - \left(\dot{Q}_{ai} + \dot{Q}_k\right)}{A} + K_i \frac{T_{\text{freezing}} - T_{\text{wall}}}{B}\right) = \\ &= \frac{1}{\rho_{i_{\text{glaze}}} L_f}\left(\frac{\dot{Q}^{\uparrow}_{\text{up}}}{A} + K_i \frac{T_{\text{freezing}} - T_{\text{wall}}}{B}\right) \end{aligned} \tag{2.27}$$

Rime-ice limit thickness

In his formulation Myers introduced the idea of an ice limit thickness in order do define the transition between the rime-ice and the glaze-ice accretion. The rime-ice limit thickness, namely B_g, is defined as the thickness at which the glaze condition first appear, therefore it is the first instant at which the water begin to accumulate on the surface. From this point on, the phenomenon is described by the glaze-ice equations.

The rime-ice limit thickness is calculated using the Stefan condition (Eq. 2.2.d) and the mass conservation law (Eq. 2.2.c) in which the water height is set to zero. Once the ice growth rate $\partial B/\partial t$ is obtained from the mass conservation law (Eq. 2.2.c) and it is substituted in the Stefan condition (Eq. 3.13), the resulting ice limit thickness is

$$B_g = \frac{AK_i \left(T_{\text{freezing}} - T_{\text{wall}}\right)}{AL_f \beta \,\text{LWC}\, V_\infty - \dot{Q}^{\uparrow}_{\text{up}}}. \tag{2.28}$$

Myers proposed to compare the ice at each time with this ice limit thickness and to use the rime or the glaze-ice accretion law depending on the cases:

- $\mathbf{B} < \mathbf{B_g}$ or $\mathbf{B_g} < \mathbf{0}$: the *rime* accretion law is used,
- $\mathbf{B} > \mathbf{B_g}$: the *glaze* accretion law is used.

This approach leads to a smooth freezing fraction function that decreases monotonically in time similarly to the Stefan predicted one in Ref. [21].

2.2.3 Modified Myers model

In the Master Thesis developed here at Politecnico di Milano by Garabelli and Gori in 2013 [27], a modified version of the Myers' model has been proposed. The modifications concern either the rime and the glaze ice condition. In the first one it is modified the mass conservation law in order to take into account the water that can flow from a neighbouring glaze cell, instead in the second one, it is proposed a new temperature profile within the ice layer. The result of these modification is reflected in a new equation for the rime-ice limit thickness B_g.

This new modified model is however based on the same hypothesis introduced by Myers shown in § 2.2.2.

Rime-ice problem

Sometimes a rime cell can collect water not only from the impinging water droplets but also from the liquid film coming from a glaze region of the surface (Fig. 2.6). This

condition is not included in the Myers' model and lead to a modification of the mass conservation law which now reads:

$$A\rho_i \frac{\partial B}{\partial t} + A\rho_w \frac{\partial h}{\partial t} = \dot{m}_d + \boldsymbol{\dot{m}^w_{in}} - \boldsymbol{\dot{m}^w_{out}} - \dot{m}_s \tag{2.29}$$

The $\dot{m}^w_\star$ terms represent the mass flux of the water flowing over the surface: the subscripted index *in* stands for the mass entering in the control domain, instead *out* stands for the mass leaving the domain. Fig. 2.6 shows the scheme used in the mass balance Eq. 2.29.

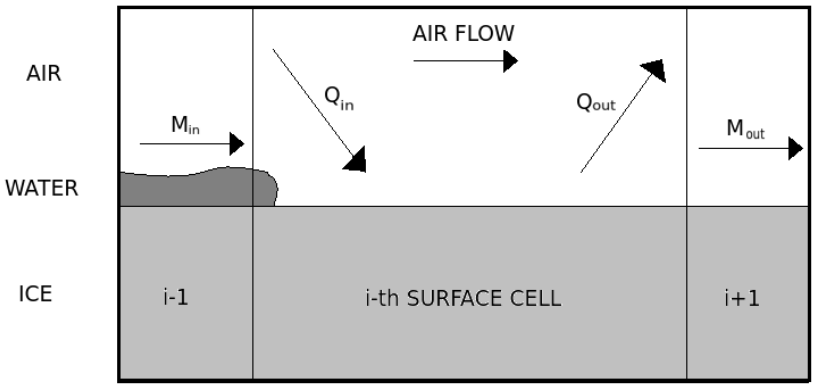

Figure 2.6: Mass balance scheme of a rime cell (i) situated near a glaze one (*i-1*).

Considering that:

- Over the surface characterized by the rime ice, the $\dot{m}^w_{out}$ is zero and
- $\frac{\partial h}{\partial t}$ is zero because, from hypothesis, when the liquid film is present it is maintained at a constant height of $1/10\ mm$,

Eq. 2.29 can be manipulated to obtain the rime-ice accretion rate:

$$\begin{aligned} \frac{\partial B}{\partial t} &= \left[\frac{\dot{m}_d + \dot{m}^w_{in} - \dot{m}_s}{A\rho_i}\right] = \\ &= \left[\frac{\beta\,\mathrm{LWC}\,V_\infty + \dot{m}^w_{in} - \dot{Q}_s/L_s}{A\rho_i}\right] \end{aligned} \tag{2.30}$$

Integrating Eq. 2.30 with the initial condition of $B_{(0)} = 0$, the ice thickness equation reads

$$\begin{aligned} B_{(t)} &= \int_0^t \left[\frac{\beta\,\mathrm{LWC}\,V_\infty + \dot{m}^w_{in} - \dot{Q}_s/L_s}{A\rho_i}\right] dt = \\ &= \left[\frac{\beta\,\mathrm{LWC}\,V_\infty + \dot{m}^w_{in} - \dot{Q}_s/L_s}{A\rho_i}\right] t \end{aligned} \tag{2.31}$$

Glaze-ice problem

In the glaze-ice condition, this model introduces a modification in the temperature distribution within the ice layer. The reason for this modification is to better respect the hypothesis of the high thermal conductivity of the wall.
The new temperature function is chosen in order to have:

- $T_{(0)} = T_{\text{wall}}$
- $T_{(B)} = T_{\text{freezing}}$
- $\frac{\partial T}{\partial z}\big|_0 \to +\infty$: at the wall the thermal flux tend to infinity due to the high thermal conductivity of the wall.

The third condition is guaranteed by the use of a function like this:

$$T_{(z)} = a\sqrt{z} + b \tag{2.32}$$

where a and b are two coefficients defined by the imposition of the first and the second constrain. This lead to the following temperature profile:

$$T_{(z)} = T_{\text{wall}} + \frac{(T_{\text{freezing}} - T_{\text{wall}})}{\sqrt{B}}\sqrt{z} \tag{2.33}$$

instead of the Myers linear one

$$T_{(z)} = T_{\text{wall}} + \frac{(T_{\text{freezing}} - T_{\text{wall}})}{B}\, z \tag{2.34}$$

In Fig. 2.7 it is shown the qualitative difference between the two profiles. It can be observed that the new profile reaches the water-ice interface with a smaller value of the $\partial T/\partial z$ derivative and this fact will influence the glaze rate accretion because of the Stefan condition. In particular the growth rate is expected to be less than Myers' one.

The analytical derivative at the interface is indeed equal to the half of the same derivative calculate with the linear temperature profile

$$\left.\frac{\partial T}{\partial z}\right|_B = \frac{(T_{\text{freezing}} - T_{\text{wall}})}{2B} \tag{2.35}$$

Following the same procedure used in the previous section, the resulting glaze-ice accretion rate calculated with the new temperature profile is

$$\begin{aligned}\frac{\partial B}{\partial t} &= \frac{1}{\rho_{i_{glaze}} L_F}\left[\frac{\left(\dot{Q}_c + \dot{Q}_e + \dot{Q}_d - \dot{Q}_k - \dot{Q}_a\right)}{A} + k_i \frac{(T_{\text{freezing}} - T_{\text{wall}})}{2B}\right] = \\ &= \frac{1}{\rho_{i_{glaze}} L_F}\left[\frac{\dot{Q}^{\uparrow}_{up}}{A} + k_i \frac{(T_{\text{freezing}} - T_{\text{wall}})}{2B}\right]\end{aligned} \tag{2.36}$$

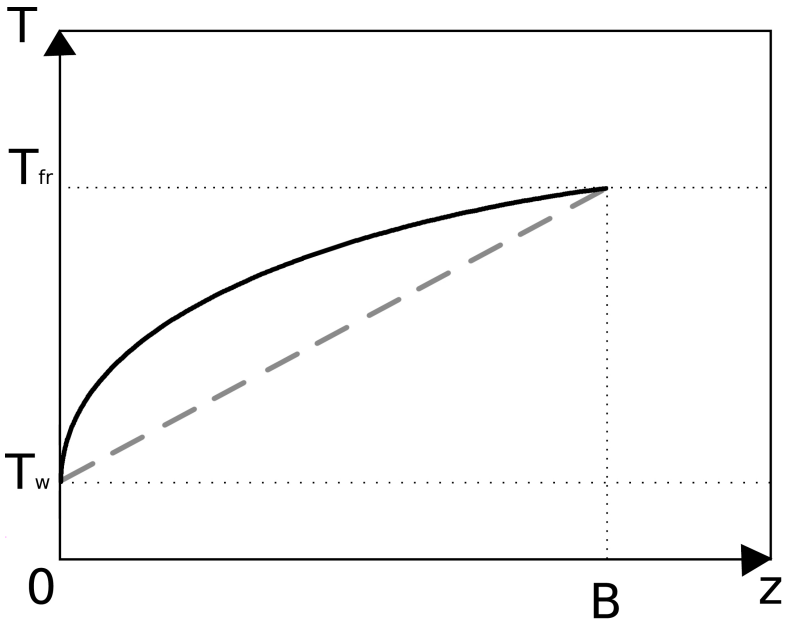

Figure 2.7: Qualitative representation of the linear temperature profile (dashed line) and the modified quadratic profile (continuous line) within the ice layer in glaze conditions.

As stated before, this modification predicts low values of the accretion rate because the second term, the one from Eq. 2.35, is the half of the corresponding Myers term in Eq. 2.27.

Rime limit thickness

The rime limit thickness is obtained substituting the equation of the mass conservation law with the $^{\partial h}/_{\partial z}$ derivative set to zero, into the Stefan condition. These two equations are here recalled:

$$\begin{cases} A\rho_i \dfrac{\partial B}{\partial t} + \cancel{A\rho_w \dfrac{\partial h}{\partial t}} = \dot{m}_d + \dot{m}_{in}^w - \dot{m}_{out}^w - \dot{m}_s \\ \rho L_F \dfrac{\partial B}{\partial t} = -K_w \dfrac{\partial \vartheta}{\partial z}\bigg|_{B(t)^+} + K_i \dfrac{\partial T}{\partial z}\bigg|_{B(t)^-} \end{cases} \tag{2.37}$$

Introducing the aeronautical parameters and the temperature derivative $^{\partial \vartheta}/_{\partial z}$ and eliminating the term $\dot{m}_{out}^w$, the resulting system is

$$\begin{cases} A\rho_i \dfrac{\partial B}{\partial t} = A\,\beta\,\mathrm{LWC}\,V_\infty + \dot{m}_{in}^w - \dot{m}_s \\ \rho_i L_F \dfrac{\partial B}{\partial t} = \dfrac{\dot{Q}_{up}^{\uparrow}}{A} + K_i \dfrac{\partial T}{\partial z} \end{cases} \tag{2.38}$$

After some manipulation and the introduction of Eq. 2.35, the rime limit thickness is

$$B_g = \frac{AK_i \left(T_{\text{freezing}} - T_{\text{wall}}\right)}{2\left[L_F\left(\beta\,\text{LWC}\,V_\infty A + \dot{m}_{in}^{w} - \dot{Q}_s/L_s\right) - \dot{Q}_{up}^{\uparrow}\right]} \tag{2.39}$$

This modified model predict a B_g that is the half of the one predicted by the original model. In this way the glaze ice condition is reached earlier and the resulting ice thickness at the end of the process is less than in the Myers model. Fig. 2.8 shows the difference between the B_g calculated with the original and the modified model. In addition, the corresponding collection efficiency distribution is reported.

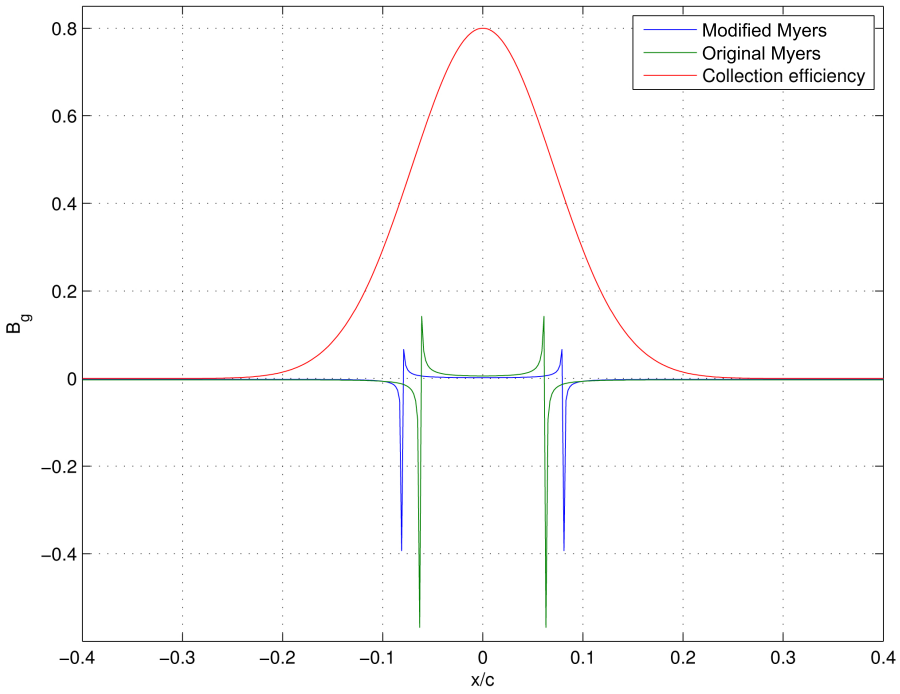

Figure 2.8: Comparison between the rime limit thickness calculated with the Myers' model and the modified model.

The assumption of a parabolic dependency on the normal coordinate to the surface is inconsistent with the temperature profile assumed in § 2.2.3. The temperature function does not respect the Fourier equation in the ice layer

$$\frac{\partial^2 T}{\partial z^2} \approx 0 \tag{2.40}$$

The second derivative of $T_{(z)} = T_{\text{wall}} + \frac{\left(T_{\text{freezing}} - T_{\text{wall}}\right)}{\sqrt{B}} \sqrt{z}$ is indeed

$$\frac{\partial^2 T}{\partial z^2} = \frac{1}{4} \frac{\left(T_{\text{freezing}} - T_{\text{wall}}\right)}{\sqrt{B}} z^{-3/2} \tag{2.41}$$

that is never zero apart for $z \to \infty$.

Apart for this aspect, this modified model provides generally better results in ice-shape prediction [27].

Chapter 3

An unsteady ice accretion model

In this chapter a novel model based on the exact solution of the Stefan problem is presented. In the *rime-ice* regime the new model closely follows the Myers formulation, however, differently from the original model, it introduces a different accretion law accounting for mass transfer occurring from a rime cell to an adjacent glaze cell (as the modified model in § 2.2.3). In the *glaze-ice* accretion the quasi-steady approximation is relaxed in order to take into account situations with fast ice accretion. In § 3.2 the exact temperature profile is derived for the first time and in § 3.3 some comparisons between the mono-dimensional quasi-steady and unsteady model are presented.
In the last section (§ 3.4) a brief summary of the models discussed up to now is proposed.

3.1 The problem

As already observed in § 2.2.2, the quasi-steady solution of the heat diffusion problem in the ice layer holds when condition 2.13 is satisfied. Although this approximation allows the heat diffusion equations to be reduced from a system of Partial Differential Equations (PDEs) to an equivalent of Ordinary Differential Equations (ODEs), in many aircraft icing applications, such as very fast wet accretions (for example in SLD conditions), the expected ice thickness does not satisfy the mentioned constraints and the initial transitory became relevant. The mentioned assumption affect the original model equations describing glaze ice growth in such a way that the models fails to predict the correct ice shape.

The starting point of the proposed formulation is the Stefan problem (Eq. 2.1), which is here recalled for ease of reference using the proper ice accretion parameters introduced in §. 1.1:

$$\begin{cases} \dfrac{\partial T}{\partial t} = \alpha_i \dfrac{\partial^2 T}{\partial z^2} \\ \dfrac{\partial \vartheta}{\partial t} = \alpha_w \dfrac{\partial^2 \vartheta}{\partial z^2} \\ \rho L_F \dfrac{\partial B}{\partial t} = -K_w \dfrac{\partial \vartheta}{\partial z}\bigg|_{B(t)^+} + K_i \dfrac{\partial T}{\partial z}\bigg|_{B(t)^-} \\ \rho_i \dfrac{\partial B}{\partial t} + \rho_w \dfrac{\partial h}{\partial t} = \beta LWCV_\infty \end{cases} \tag{3.1}$$

The subscripted index i and w stands for the *ice* and the *water* phase respectively and $\alpha_\star = \frac{K_\star}{\rho_\star C_\star}$ represent the thermal conductivity of the ice or the water. The reference system is reported in Fig. 2.2 and typical values of the coefficients are reported in Tab. 2.2.

As already discussed in § 2.2.2, aeronautical working conditions are such that the water film is nearly everywhere very thin (around 1/10 mm), thus justifying the assumption of infinite conduction through the water. According to this hypothesis, the temperature of the liquid film can be considered approximately constant and equal to the freezing temperature of water. In the present formulation, the water layer is supposed to be infinitesimally thin, so that it can be assimilated to an interface where to impose the Dirichlet boundary conditions. In this context, the Fourier equation in the water layer is discarded and the complete Stefan problem is reduced to:

$$\begin{cases} \dfrac{\partial T}{\partial t} = \alpha_i \dfrac{\partial^2 T}{\partial z^2} \\ \rho L_F \dfrac{\partial B}{\partial t} = -K_w \dfrac{\partial \vartheta}{\partial z}\bigg|_{B(t)^+} + K_i \dfrac{\partial T}{\partial z}\bigg|_{B(t)^-} \\ \rho_i \dfrac{\partial B}{\partial t} + \rho_w \dfrac{\partial h}{\partial t} = \beta LWCV_\infty \end{cases} \tag{3.2}$$

3.2 Similarity solution in glaze-ice conditions

An unsteady exact solution for the above simplified Stefan problem is deduced using a similarity approach (like in [28] and [29]) in order to determine the temperature profile in the ice layer and the glaze-ice accretion rate. Similarity approach means that the initial problem is changed to a problem of only one variable made by the combination of other variables and the solution is everywhere the same (same shape) but with a different scale factor.
Solving the Fourier equation in the ice layer by means of a similarity solution requires that the boundary conditions satisfy certain properties, for example it can be imposed a constant value of the temperature or a heat flux proportional to the $\sqrt{t}$ (see [29]). In this work the temperatures at the wall and at the ice-water interface are specified.
For this reason this approach is applied in the *glaze-ice condition* because the temperature

at the ice-water interface is supposed to be fixed (in time) and equal to the freezing temperature. Similarly to Myers model (§ 2.2.2), the two Dirichlet boundary conditions for temperature read:

$$T_{(0,t)} = T_{\text{wall}} \tag{3.3a}$$

$$T_{(B(t),t)} = T_{\text{freezing}} \tag{3.3b}$$

The heat diffusion equation in the ice layer is a PDE function of space and time and it is reduced to a more simple ODE thanks to the definition of the following similarity variable:

$$\xi_{(z,t)} = \frac{z}{\sqrt{t}} \tag{3.4}$$

The temperature profile in the ice layer is now expressed in terms of the only similarity variable ξ as a combination of z and t:

$$T_{(z,t)} \rightarrow \Theta\big(\xi_{(z,t)}\big) \tag{3.5}$$

Using the chain rule of derivation, the time and space derivatives of $T_{(z,t)}$ can be expressed as function of ξ as:

$$\frac{\partial T}{\partial t} = \frac{\partial T}{\partial \xi}\,\frac{\partial \xi}{\partial t} = -\frac{x}{2t\sqrt{t}}\,\Theta'_{(\xi)} = -\frac{\xi}{2t}\,\Theta'_{(\xi)} \tag{3.6a}$$

$$\frac{\partial^2 T}{\partial z^2} = \frac{\partial^2 T}{\partial \xi^2}\,\frac{\partial^2 \xi}{\partial z^2} = \frac{1}{t}\,\Theta''_{(\xi)} \tag{3.6b}$$

which substituted into 3.2.a, the heat equation in the ice layer becomes:

$$-\Theta'_{(\xi)}\,\frac{\xi}{2t} = \alpha_i\,\Theta''_{(\xi)}\frac{1}{t}$$

$$2\,\alpha_i\,\Theta''_{(\xi)} + \xi\,\Theta'_{(\xi)} = 0. \tag{3.7}$$

Defining the parameter $M_{(\xi)} = C_1\,e^{\xi^2/4\alpha_i}$ it can be demonstrated that Eq. 3.7 is equivalent to

$$\frac{\partial}{\partial \xi}\left(M_{(\xi)}\,\frac{\partial \Theta_{(\xi)}}{\partial \xi}\right) = 0 \tag{3.8}$$

whose solution is:

$$\Theta_{(\xi)} = A\int_0^{\xi} \exp\left(-\frac{s^2}{4\alpha_i}\right)\mathrm{d}s + D$$

$$\Theta_{(\xi)} = A\,\mathrm{erf}\left(\frac{\xi}{2\sqrt{\alpha_i}}\right) + D \tag{3.9}$$

A and D are two integration constants which have to be determined by applying the boundary conditions in 3.3, so:

$$T_{(0,t)} = T_{\text{wall}} \quad \longrightarrow \quad D = T_{\text{wall}} \tag{3.10a}$$

$$T_{(B(t),t)} = T_{\text{freezing}} \quad \longrightarrow \quad A = \frac{T_{\text{freezing}} - T_{\text{wall}}}{\text{erf}(\lambda)} \tag{3.10b}$$

where

$$\lambda = \frac{B(t)}{2\sqrt{\alpha_i t}} \tag{3.11}$$

Substituting the integration constant Eq. 3.10 and the definition of ξ (Eq. 3.4) in Eq. 3.9 it yields the exact temperature profile the ice layer:

$$T_{(z,t)} = T_{\text{wall}} + (T_{\text{freezing}} - T_{\text{wall}}) \frac{\text{erf}\left(\dfrac{z}{2\sqrt{\alpha_i t}}\right)}{\text{erf}(\lambda)} \tag{3.12}$$

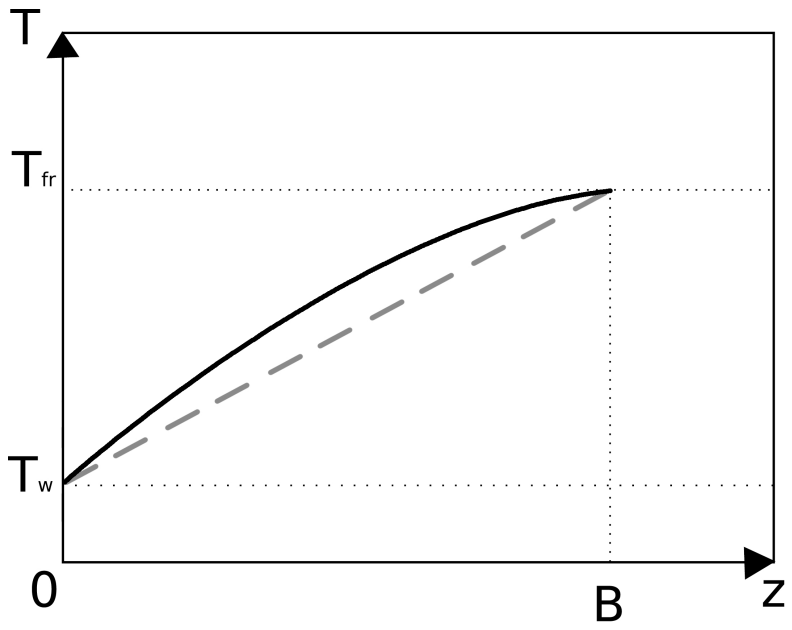

Figure 3.1: Qualitative representation of the linear temperature profile (dashed line) and the exact temperature profile (continuous line) within the ice layer in glaze conditions.

The temperature solution deduced right now is not actually a well defined solution because it depends on the interface position $B_{(t)}$ which is still unknown. $B_{(t)}$ appears indeed in the definition of the parameter λ (Eq. 3.11).

In order to close the problem, the Stefan condition (Eq. 3.13) is now applied and after some manipulation, this leads to a non-linear equation in λ, which needs to be solved to determine the unknown position of the ice-water interface.

The procedure that allows to retrieve $B_{(t)}$ and the accretion rate $^{\partial B}/_{\partial t}$ starts from the calculation of the derivatives of the temperature and of the position of the ice-water interface involved in the Stefan condition. The Stefan condition is here recalled for convenience:

$$\rho L_F \frac{\partial B}{\partial t} = -K_w \frac{\partial \vartheta}{\partial z}\bigg|_{B(t)^+} + K_i \frac{\partial T}{\partial z}\bigg|_{B(t)^-}. \tag{3.13}$$

1. **Calculation of the temperature gradient $\frac{\partial \vartheta}{\partial z}\big|_{B(t)^+}$ in the water layer at the interface**

   The calculation of the temperature gradient in the water layer at the interface requires initially to analyse the thin film approximation discussed in § 2.2.2. Following Myers [11], it is assumed that if

   $$\hat{h} \ll \frac{K_w}{\phi\beta\,\mathrm{LWC}\,V_\infty C_w} \tag{3.14}$$

   the heat equation in the water layer (Eq. 2.1b) reduces to the leading-order quasi-steady problem

   $$\frac{d^2\vartheta}{dz} \approx 0 \qquad \text{with } 0 < z < h, \tag{3.15}$$

   which, integrated with the appropriate boundary condition $T_{(0)} = T_f$, yields to a linear temperature profile in the water layer of the form

   $$\vartheta_{(z)} = \frac{d\vartheta}{dz} z + T_f \tag{3.16}$$

   Being $\vartheta_{(z)}$ a linear function of z, it follows that:

   $$\frac{\partial \vartheta}{\partial z}\bigg|_{B(t)^+} = \frac{\partial \vartheta}{\partial z}\bigg|_{B(t)+h(t)} \tag{3.17}$$

   and the heat balance at the water-air interface reads:

   $$\begin{aligned} -K_w \frac{\partial \vartheta}{\partial z}\bigg|_{B(t)^+} &= \left(\dot{Q}_{cw} + \dot{Q}_e\right) + \dot{Q}_d - \left(\dot{Q}_{aw} + \dot{Q}_k\right) = \\ &= \bar{H}_1 \left(\vartheta_{(h,t)} - T_{\mathrm{local}}\right) + \bar{H}_2 \left(\vartheta_{(h,t)} - T_\infty\right) - \left(\dot{Q}_{aw} + \dot{Q}_k\right) = \\ &\triangleq \dot{Q}^{\uparrow *}_{\mathrm{up}} \end{aligned} \tag{3.18}$$

   where $\bar{H}_1 = \left(\bar{H}_{aw} + \chi e_0\right)$ and $\bar{H}_2 = \beta\,\mathrm{LWC}\,V_\infty C_w$. Differently from Myers formulation [11], the heat fluxes expressing the heat exchanged by convection and by evaporation at the water-air interface include the local temperature of the airflow outside the boundary layer instead of the free-stream temperature:

   $$\dot{Q}_{cw} = \bar{H}_{aw} \left(\vartheta_{(h,t)} - T_{\mathrm{local}}\right) \tag{3.19a}$$

   $$\dot{Q}_e = \chi \left[e\left(\vartheta_{(h,t)}\right) - e_{(T_{\mathrm{local}})}\right] \approx \chi e_0 \left(\vartheta_{(h,t)} - T_{\mathrm{local}}\right) \tag{3.19b}$$

The importance of using of the local temperature instead of the free-stream static temperature will be discussed in Ch. 4.

Substituting Eq. 3.16 into Eq. 3.18 yields:

$$-\left.\frac{\partial\vartheta}{\partial z}\right|_{B(t)^+} = \frac{\bar{H}_1\left(T_{\text{freezing}} - T_\infty\right) + \bar{H}_2\left(T_{\text{freezing}} - T_{\text{local}}\right) - \left(\dot{Q}_{aw} + \dot{Q}_k\right)}{K_w + \left(\bar{H}_1 + \bar{H}_2\right) h_{(t)}} \tag{3.20}$$

The thin film approximation that holds for typical aeronautical conditions ($h_{(t)} \approx 1/10$ mm and $\vartheta \approx T_{\text{freezing}}$ everywhere) is now introduced and the term $\left(\bar{H}_1 + \bar{H}_2\right) h_{(t)}$ in Eq. 3.21 is neglected with respect to K_w. Hence, the final form of the temperature gradient at the water-air interface is

$$\begin{aligned} -\left.\frac{\partial\vartheta}{\partial z}\right|_{B(t)^+} &\approx \frac{\bar{H}_1\left(T_{\text{freezing}} - T_\infty\right) + \bar{H}_2\left(T_{\text{freezing}} - T_{\text{local}}\right) - \left(\dot{Q}_{aw} + \dot{Q}_k\right)}{K_w} = \\ &= \frac{\dot{Q}^{\uparrow *}_{\text{up}}}{K_w} \end{aligned} \tag{3.21}$$

2. **Calculation of the temperature gradient $\left.\frac{\partial T}{\partial z}\right|_{B(t)^-}$ in the ice layer at the interface**

The derivation of the exact temperature profile (Eq. 3.12) in the ice layer at the interface leads to

$$\begin{aligned} \frac{\partial T}{\partial z} &= \frac{\left(T_{\text{freezing}} - T_{\text{wall}}\right)}{\operatorname{erf}(\lambda)} \frac{2}{\sqrt{\pi}} \frac{d}{dz}\left[\int_0^{\frac{z}{2\sqrt{\alpha_i t}}} e^{-y^2}\, dy\right] = \\ &= \frac{\left(T_{\text{freezing}} - T_{\text{wall}}\right)}{\operatorname{erf}(\lambda)} \frac{\exp\left(-\left(\frac{z}{2\sqrt{\alpha_i t}}\right)^2\right)}{\sqrt{\pi\alpha_i t}} \end{aligned} \tag{3.22}$$

that evaluated in $z = B_{(t)}{}^-$ leads to the temperature gradient in the ice layer at the ice-water interface:

$$\left.\frac{\partial T}{\partial z}\right|_{B(t)^-} = \frac{\left(T_{\text{freezing}} - T_{\text{wall}}\right)}{\operatorname{erf}(\lambda)} \frac{\exp\left(-\lambda^2\right)}{\sqrt{\pi\alpha_i t}} \tag{3.23}$$

3. **Calculation of the accretion rate from the exact temperature solution**

   Recalling Eq. 3.11, the position of the water-ice interface reads

$$B(t) = 2\lambda\sqrt{\alpha_i t}, \tag{3.24}$$

   so the accretion rate can be expressed as function of λ

$$\frac{\partial B}{\partial t} = \lambda\sqrt{\frac{\alpha_i}{t}} \tag{3.25}$$

Combining Eq. 3.21, Eq. 3.23 and Eq. 3.25 in the Stefan condition (Eq. 3.13) the result is a non-linear equation in the unknown λ:

$$L_f\rho_i\sqrt{\frac{\alpha_i}{t}}\lambda - K_i\frac{(T_{\text{freezing}} - T_{\text{wall}})}{\text{erf}(\lambda)}\frac{\exp\left(-\lambda^2\right)}{\sqrt{\pi\alpha_i t}} - \dot{Q}^{\uparrow *}_{\text{up}} = 0 \tag{3.26}$$

An iterative procedure for the solution of the above equation, like a Newton-Raphson method, yields the value of λ, from which it can be retrieved $B_{(t)}$.
The accretion rate results trivially from the substitution of the interface derivative (Eq. 3.23 and Eq. 3.21) into the Stefan condition (Eq. 3.13) and the inclusion of the parameter λ just computed:

$$\rho L_F\frac{\partial B}{\partial t} = -K_w\frac{\partial\vartheta}{\partial z}\bigg|_{B(t)^+} + K_i\frac{\partial T}{\partial z}\bigg|_{B(t)^-}$$

$$\frac{\partial B}{\partial t} = \frac{1}{\rho_{i_{\text{glaze}}} L_f}\left(K_i\frac{(T_{\text{freezing}} - T_{\text{wall}})}{\text{erf}(\lambda)}\frac{\exp\left(-\lambda^2\right)}{\sqrt{\pi\alpha_i t}} + \dot{Q}^{\uparrow *}_{\text{up}}\right) \tag{3.27}$$

Finally, integrating in time with the initial condition $B_{(0)} = 0$ it is therefore obtained the ice thickness at time t:

$$B_{(t)} = \frac{1}{\rho_{i_{\text{glaze}}} L_f}\left(K_i\frac{(T_{\text{freezing}} - T_{\text{wall}})}{\text{erf}(\lambda)}\frac{\exp\left(-\lambda^2\right)}{\sqrt{\pi\alpha_i t}} + \dot{Q}^{\uparrow *}_{\text{up}}\right) t \tag{3.28}$$

In practical applications, such as in the ice accretion software PoliMIce that will be introduced in §. 5.1.3, the ice accretion problem is discretized in time, so the thickness of the ice layer at the current time step can be calculated by means of an explicit Forward Euler Algorithm

$$B\left(t_{n+1}\right) = B^{(n+1)} = B^{(n)} + \frac{\partial B}{\partial t}\bigg|^{(n)}\Delta t \tag{3.29}$$

In the same way, the glaze-ice accretion rate is evaluated on the basis of the ice thickness – and hence the parameter λ – related to the previous time step:

$$\lambda^n = \frac{B^{(n-1)}}{2\sqrt{\alpha_i t^{(n-1)}}} \tag{3.30}$$

and

$$\left.\frac{\partial B}{\partial t}\right|^{(n)} = \frac{1}{\rho_{i_{\text{glaze}}} L_f}\left(K_i \frac{(T_{\text{freezing}} - T_{\text{wall}})}{\text{erf}(\lambda^{(n)})} \frac{\exp\left(-\left(\lambda^{(n)2}\right)\right)}{\sqrt{\pi \alpha_i t^{(n)}}} + \dot{Q}_{\text{up}}^{\uparrow *\,(n)}\right) \tag{3.31}$$

Rime-ice limit thickness

Following Myers' approach [11], the criterion allowing to discern whether the rime or glaze accretion law is to be employed is based on the definition of the rime limit thickness. As already discussed in §. 2.2.2, the rime limit thickness B_g is the maximum rime ice thickness, beyond which only the glaze ice can grow. According to the formulation presented in the aforementioned section, the rime limit thickness results from the substitution of the mass balance equation 3.2c, with h set to zero, into the Stefan condition (Eq. 3.13). A non-linear equation in λ, is obtained:

$$\frac{1}{\rho_i}\beta\,\text{LWC}\,V_\infty - K_i \frac{(T_{\text{freezing}} - T_{\text{wall}})}{\text{erf}\,(\lambda)} \frac{\exp\left(-\lambda^2\right)}{\sqrt{\pi \alpha_i t}} - \dot{Q}_{\text{up}}^{\uparrow *} = 0 \tag{3.32}$$

As before, λ is calculated with an iterative method and then the limiting thickness B_g can be obtained substituting λ in Eq. 3.24.

Similarly of the ice thickness B and the ice accretion rate $^{\partial B}/_{\partial t}$, the non-linear Eq. 3.32 is not solved but it is used the modified version of the ice thickness limit described in § 2.2.3 because it is faster and more robust.
It is here recalled:

$$B_g = \frac{AK_i\,(T_{\text{freezing}} - T_{\text{wall}})}{2\left[L_f\left(\beta\,\text{LWC}\,V_\infty A - {}^{\dot{Q}_s}/_{L_s}\right) - \left(\dot{Q}_c + \dot{Q}_s + \dot{Q}_d - \dot{Q}_k - \dot{Q}_a\right)\right]} \tag{3.33}$$

3.3 Comparison between the models

In this section some comparisons between the Myers model and the exact solution are discussed.

As demonstrated at the beginning of the previous section, Eq. 3.12 shows how the temperature profile within the ice layer depends on the combination of time and the final thickness (B). For this reason it can be said that the behaviour of the function is related to the (mean) ice accretion rate.
The temperature profiles are recalled in the following Tab. 3.1:

Model	$\boldsymbol{T(z,t)}$
Myers	$T_{\text{wall}} + \dfrac{(T_{\text{freezing}} - T_{\text{wall}})}{B} z$
Unsteady exact solution	$T_{\text{wall}} + (T_{\text{freezing}} - T_{\text{wall}}) \dfrac{\text{erf}\left(\dfrac{z}{2\sqrt{\alpha_i t}}\right)}{\text{erf}(\lambda)}$

Table 3.1: Temperature profile within the glaze-ice layer using the Myers model or the exact unsteady solution.
The λ parameter was defined in Eq. 3.11 as $\lambda = \frac{B(t)}{2\sqrt{\alpha_i t}}$

In order to perform some comparisons between the exact temperature profile and the liner Myers profile in glaze conditions, some values of t and B are imposed in Eq. 3.12. Figure 3.2 shows 4 different temperature profiles in 4 different conditions. The temperature profiles were obtained considering a fixed value of 2 cm for the ice thickness and 4 different value of the accretion time: 100, 200, 300, and 400 seconds. These values were chosen in order to represent the SLD cases from the NASA report in reference [9] (based on the cases 080395) and they are reported in Tab. 3.2:

Case	**Time** $[s]$	**Ice thickness** $[m]$	**Mean accretion rate** $[m/s]$
(a)	100	0.02	$2 \cdot 10^{-4}$
(b)	200	0.02	$1 \cdot 10^{-4}$
(c)	300	0.02	$0.6 \cdot 10^{-4}$
(d)	400	0.02	$0.5 \cdot 10^{-4}$

Table 3.2: Values of the accretion rates used in Fig. 3.2.

The exact temperature profiles collapse to the Myers linear profile for low values of the accretion rate, instead the two profiles are more and more different when the accretion rate increase. It means that the unsteady correction of the Myers model is more significant in situations of fast ice growth.
The departure from the linearity affect especially the values of the temperature derivative

at the wall and at the ice-water interface. The first one represents the heat flux conduced from the wall, whereas the second one is related to the speed at which the interface moves (Eq. 3.13).

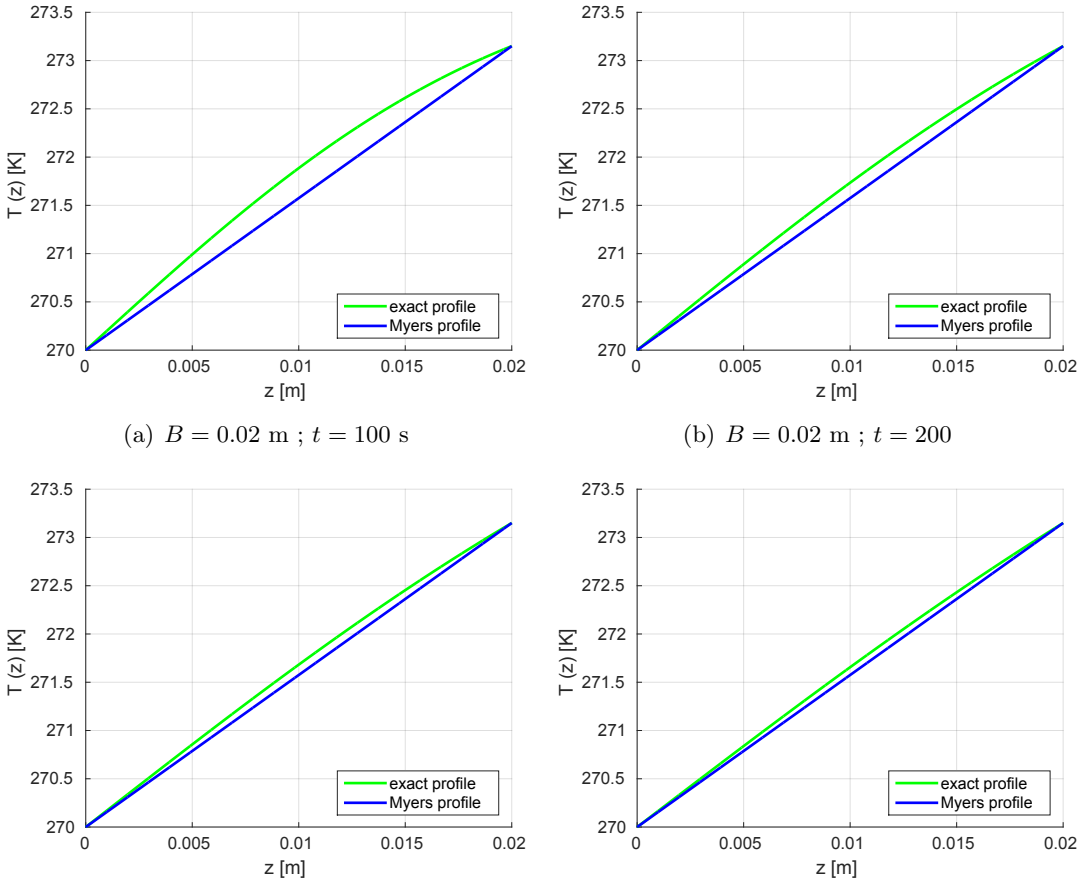

(a) $B = 0.02$ m ; $t = 100$ s

(b) $B = 0.02$ m ; $t = 200$

(c) $B = 0.02$ m ; $t = 300$ s

(d) $B = 0.02$ m ; $t = 400$ s

Figure 3.2: Comparisons between the linear temperature profile predicted by the Myers model and the exact unsteady one. The outside air temperature is 270 K, the ice thickness is 2 cm and the accretion time varies from 100 to 400 seconds.

In Tab. 3.3 are reported the percentage errors between the derivative at the wall and at the interface. This difference is calculated as

$$\Delta_{\%} = \frac{\left(\left.\frac{\partial T}{\partial z}\right|_{Myers} - \left.\frac{\partial T}{\partial z}\right|_{exact} \right)}{\left.\frac{\partial T}{\partial z}\right|_{Myers}} \tag{3.34}$$

so, positive values mean that the Myers' function is steeper than the exact one.

Case	$\Delta_{\%}^{\text{wall}}$	$\Delta_{\%}^{\text{interf.}}$
(a)	-28.04%	$+44.05\%$
(b)	-13.95%	$+24.67\%$
(c)	-9.27%	$+17.08\%$
(d)	-6.94%	$+13.05\%$

Table 3.3: Errors in the derivative values at the wall and at the interface between the Myers model and the exact solution.

The error committed by the Myers model is reported in Fig. 3.3 and, as seen in Tab. 3.3 it is usually positive at the interface and negative at the wall, therefore with a linear temperature profile, the derivative at the wall is under-estimated whereas it is over-estimated at the interface.

In atmospheric conditions providing a very fast ice growth, the importance of this discrepancy between the two models may become relevant. For example, in situations like the previous one, an anti-icing system designed with the Myers model results to be under-dimensioned because the heat flux at the wall is the $20 \div 30$ % less then the needed one.

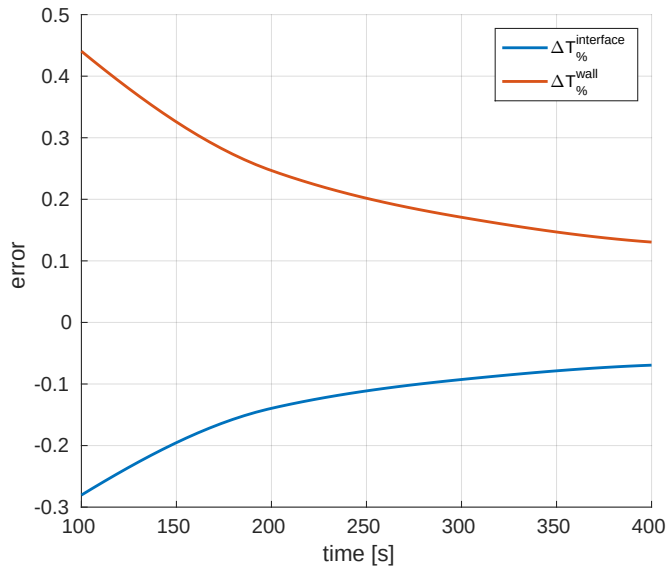

Figure 3.3: Error between the derivative computed with the linear temperature profile and the exact unsteady temperature profile at the wall (red) and at the interface (blue).

3.4 Summary

In this section, a brief summary of the models explained in this chapter is given and the main differences among each others are summarized in Tab. 3.4 for clarity.

Model	$\boldsymbol{T_{air}}$	$\boldsymbol{\dot{m}_{in}^{w}}$	$\boldsymbol{T_{glaze}(z)}$
Myers	T_∞	no	Linear: $T_{(z)} \propto z$
Modified Myers	T_∞	yes	Quadratic: $T_{(z)} \propto \sqrt{z}$
Unsteady	T_{local}	yes	Exact: $T_{(z)} \propto erf(z)$

Table 3.4: Summary of the main characteristics of the models presented in the previous sections.

The Stefan problem is the starting point to derive these models. The main hypothesis used to derive the Myers model is the use of a quasi-steady approach which lead to a linear temperature profile within the glaze-ice layer. The mathematical formulation is consistent with its hypothesis but it is not able to represent the high conductivity of the wall. In order to solve this problem a modified version of the Myers model has been proposed in a master theses here at Politecnico di Milano. The modification consists in the imposition of a quadratic temperature profile within the glaze-ice layer with infinite derivative at the wall. In this model a modification of the mass balance equation is also introduce. In this way, the water flowing from a glaze cell to a rime one is now considered. This model is however not consistent with its hypothesis, the second derivative of the temperature is indeed not equal to zero. In the last model it is considered the Stefan problem with its unsteady part and the exact temperature profile in the glaze-ice is deduced with a similarity approach. Moreover, in this model it is performed a correction in the temperature field with the introduction of the *local temperature* field which will be better described in Ch. 4. These models differ also to each other in the rime limit thickness. The introduction of the aforementioned hypothesis lead to three different equations for the computation of the B_g. However, the unsteady model in practical application uses the modified version of the B_g.

From now on, the unsteady model with the local temperature correction and the contribution of the $\dot{m}_{in}^{w}$ in the mass equation law is also called "PoliMIce model".

Chapter 4

Local temperature correction

The new unsteady model derived in Ch.3 is now improved by considering the local value of the temperature along the airfoil, instead of the upstream static temperature considered in both the Myers and the improved Myers models. In § 4.1 the definition of *local temp* is given and in § 4.2 the heat fluxes are corrected with the introduction of the local temperature. In § 4.3 the isentropic relations used to reconstruct the local temperature field are recalled and in § 4.3 a numerical simulation is performed on a test case to show the comparison between the local temperature field and the upstream static temperature. The isentropic relations are used to compute the temperature field from the total temperature and the local value of the velocity.

4.1 The *local temperature*

Ice accretion growth is a process very sensitive to the temperature, for example, as shown in Ch. 2, a change of few degrees in air temperature can lead to a different kind of ice accretion: rime or glaze. These conditions are governed by two different accretion laws and so, at the end of the process, the resulting ice shape (and ice thickness) may be very different. An accurate description of the temperature field is important in the evaluation of the heat fluxes involved in the heat balance equation.
The temperature near the surface is different from point to point because air is a compressible fluid and then is subjected to temperature variation related to changes in pressure and density. This variation is therefore strictly related to the velocity field generated by the geometry of the body, and it is very important also at low velocities. From the energy conservation law, regions with high velocities are related to lower temperature while, on the other side, regions with low velocities are related to higher temperature. The maximum value in temperature is reached at the stagnation point because the velocity is zero.

The term *local temperature* represent the air temperature near the surface just outside the thermal boundary layer. The thermal boundary layer, like the velocity (or viscous) boundary layer, is a thin layer of air surrounding the surface in which the viscosity effects are not negligible. In this volume the temperature changes along the normal direction

from the surface temperature to the upstream temperature T_∞ (Fig. 4.1(a)). In this work, due to the importance of the compressibility effects, the static temperature outside the boundary layer is replaced by the so-called *local temperature*, so the asymptotic temperature T_∞ in Fig. 4.1(a) is replaced with the *local temperature*.

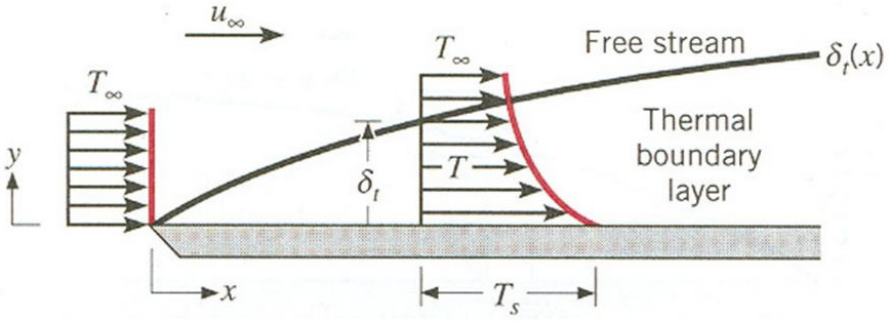

(a) Temperature profile within the thermal boundary layer.

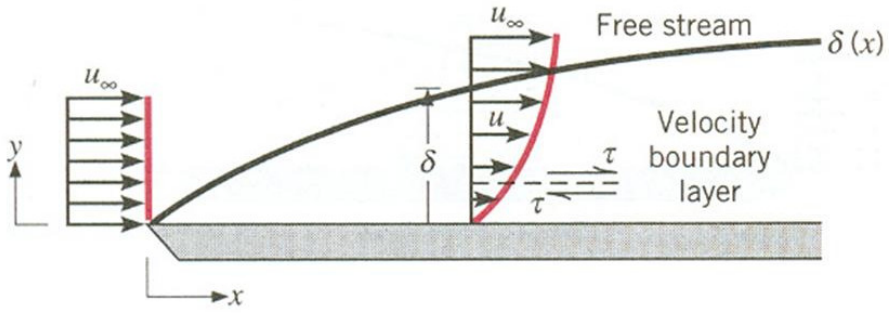

(b) Velocity profile within the viscous boundary layer.

Figure 4.1: Viscous and thermal boundary layers.

The thickness of the thermal boundary layer is ruled by the Prandtl number, this is a dimensionless number representing the relation between the viscous diffusion rate (ν) and the thermal diffusion rate (α) and its value is a characteristic of the considered medium.

$$\mathrm{Pr} = \frac{\nu}{\alpha} = \frac{c_p \mu}{k} \tag{4.1}$$

$\nu = \mu/\rho$ is the kinematic viscosity, $\alpha = k/\rho_a c_p$ is the thermal diffusivity, k is the thermal conductivity, c_p is the specific heat and ρ_a is the density of the air. A typical value for the Prandtl number in air is around $0.7 \div 0.8$.
When Pr is less than 1, it means that the heat diffuses quickly compared to the velocity, therefore it gives also informations about the thickness relation between the velocity boundary layer and the heat boundary layer.

- **Pr < 1** means that the thermal diffusivity dominates, so $\delta_\mathrm{T} > \delta_\nu$

- **Pr = 1** means that the thermal and the viscous diffusivity are equivalent, so $\delta_T = \delta_\nu$
- **Pr > 1** means that the viscous diffusivity dominates, so $\delta_\mathrm{T} < \delta_\nu$

where δ_T is the thermal boundary layer and δ_ν is the viscous boundary layer. These different behaviours are summarized in Fig. 4.2.
A more accurate realation between δ_ν and δ_T is given by equation

$$\frac{\delta_\nu}{\delta_\mathrm{T}} \approx \mathrm{Pr}^{1/3} \tag{4.2}$$

With the Prandtl number in air, this ratio is around $0.88 \div 0.93$, so the two boundary layers can be considered approximately the same height.
With this approximation, the local temperature chosen for the computation of the heat fluxes becomes the temperature just outside the viscous boundary layer.

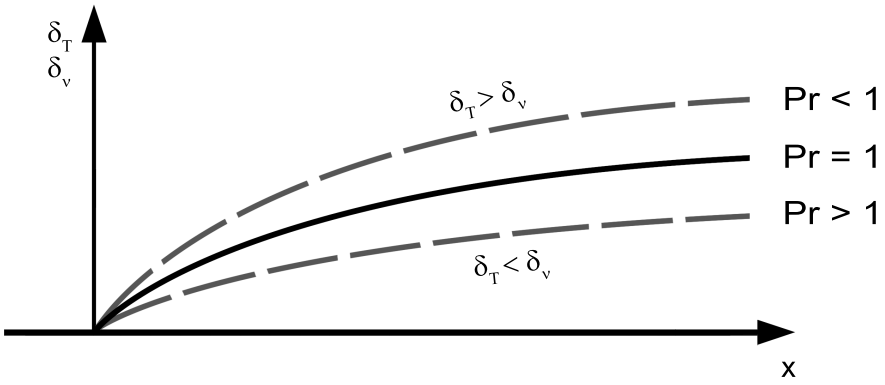

Figure 4.2: Thermal boundary layer thickness in relation to the viscous boundary layer and the Prandtl number.

4.2 Thermal fluxes correction

The heat fluxes introduced in § 2.2.2 which exchange heath with the atmosphere are all related to the upstream static temperature, therefore the temperature is uniform in the entire flow field thus the value heat exchanged at each point over the surface relies on the same value of temperature.
The thermal fluxes that can be corrected including the *local temperature* are the convective heat flux, the evaporative heat flux and the sublimation heat flux:

- $\dot{Q}_{c\star} = h_{c\star}(T - T_\infty)\, A \quad \longrightarrow \quad \dot{Q}_{c\star} = h_{c\star}(T - T_{\mathbf{local}})\, A$
- $\dot{Q}_{e,s} = \chi_{e,s}\, e_0\, (T - T_\infty)\; A \quad \longrightarrow \quad \dot{Q}_{e,s} = \chi_{e,s}\, e_0\, (T - T_{\mathbf{local}})\; A$

In this way each point on the surface exchanges heat towards a different air temperature. These new fluxes definitions are used in the heat balance equation.

4.3 Reconstruction of the temperature field

In this section it is explained how to reconstruct the temperature field starting from the pressure distribution. If a compressible computation is available the temperature field is directly given, otherwise it is reconstructed using the isentropic relations.

At high Reynolds numbers, the flow field around a surface my be split in two region with different properties: the boundary layer and the external flow. In the first region the fluid is rotational ($\nabla \times \mathbf{u} \neq 0$) because the viscous forces dominate the flow behaviour, whereas, on the other hand, the external flow can be considered inviscid because the inertial forces dominates over the viscous ones. From the Crocco equation

$$(\nabla \times \mathbf{u}) \times \mathbf{u} = T\nabla s - \nabla H \tag{4.3}$$

can be seen that an irrotational fluid with constant total enthalpy is also isentropic along the streamlines (Eq. 4.4), therefore the temperature field can be reconstruct using the isentropic relations.

$$\cancel{\mathbf{u} \cdot [(\nabla \times \mathbf{u}) \times \mathbf{u}]} = \mathbf{u} \cdot (T\nabla s) - \cancel{\mathbf{u} \cdot \left[\nabla \left(h + \frac{V^2}{2}\right)\right]}$$

$$\mathbf{u} \cdot (T\nabla s) = 0 \tag{4.4}$$

In compressible and steady-state conditions,

$$\mathbf{u} \cdot \nabla \left(h + \frac{V^2}{2}\right) = 0 \tag{4.5}$$

where $\mathbf{u}$ is the velocity vector, V is its module and h is the specific enthalpy.
This equation shows that the quantity $\left(h + \frac{V^2}{2}\right)$ has no variation in the direction of $\mathbf{u}$, so

$$h + \frac{V^2}{2} = const \tag{4.6}$$

over a given streamline.
On the other hand, in incompressible flows Eq. 4.6 reduces to

$$P + \frac{1}{2}\rho V^2 = const \tag{4.7}$$

over a given streamline. This equation is particularly important in this work because the aerodynamic solver used to perform the simulations in Ch. 5 is a steady-state incompressible solver.

During an isentropic transformation

$$Pv^{\gamma} = \text{const} \tag{4.8}$$

where v is the specific volume ($v = 1/\rho$) and γ is the ratio of the specific heat calculated at constant pressure and constant volume ($\gamma = c_p/c_v$). From Eq. 4.8, after some manipulations and the introduction of the stagnation quantities T_0 and P_0, it is deduced the isentropic relation between temperature and pressure:

$$\frac{P}{P_0} = \left(\frac{T}{T_0}\right)^{\frac{\gamma}{\gamma-1}} \tag{4.9}$$

This is the equation used to reconstruct the temperature field $T_{(x,y,z)}$:

$$T = T_0 \left(\frac{P}{P_0}\right)^{\frac{\gamma-1}{\gamma}} \tag{4.10}$$

where T and P are functions of the position: $T = T_{(x,y,z)}$ and $P = P_{(x,y,z)}$.

The stagnation quantities are obtained bringing the fluid to the rest along an isentropic process and remain constant within the flow field. P_0 is obtained from the Bernoulli's Eq. 4.7,

$$P_0 = P + \frac{1}{2}\rho V^2 \tag{4.11}$$

while T_0 is obtained introducing the definition of the enthalpy $h = c_p T$ in Eq. 4.6:

$$T_0 = T + \frac{V^2}{2c_p} \tag{4.12}$$

Numerical simulations

Two simulations were performed at 0 (clean surface) and 360 seconds (iced surface) with the data reported in Tab. 4.1.

Fig. 4.3(b) and Fig. 4.4(b) show the ΔT between the local temperature computed using Eq. 4.10 and the free stream temperature T_∞: $\Delta T = (localTemp - T_\infty)$.

$\boldsymbol{\alpha}$ [deg]	$\boldsymbol{V_\infty}$ [m/s]	$\boldsymbol{T_\infty}$ [K]	$\boldsymbol{P_\infty}$ [Pa]	**chord** [m]
4	67	267.6	95000	0.53

Table 4.1: Flight conditions for the reference case

Fig. 4.3 and Fig. 4.4 highlight the relation between the flow field and the temperature field anticipated at the beginning of this section. Regions of high velocities are related to regions of low temperatures and vice versa. Moreover the temperature at the stagnation

point reaches the maximum within the temperature field. The difference between the maximum and the minimum temperature in the temperature field is around 4 degrees at 0 seconds and 6 degrees after 360 seconds. The increase of this gap is due to the irregular shape of the ice accretion which introduces more regions of high velocities. Ice shape in Fig. 4.4 shows the accretion of two "horns" where the local temperature is less than the asymptotic one, in particular in the upper side of the airfoil this horn is wider than the lower one. On the other hand at the stagnation point the ice accretion has a "hole" and it shows its minimum thickness due to the maximum temperature in the temperature field.

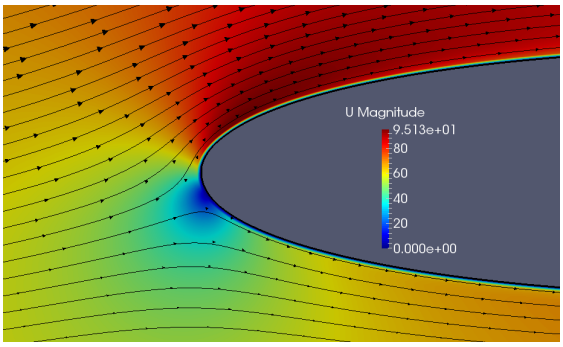

(a) Flow field at 0 s

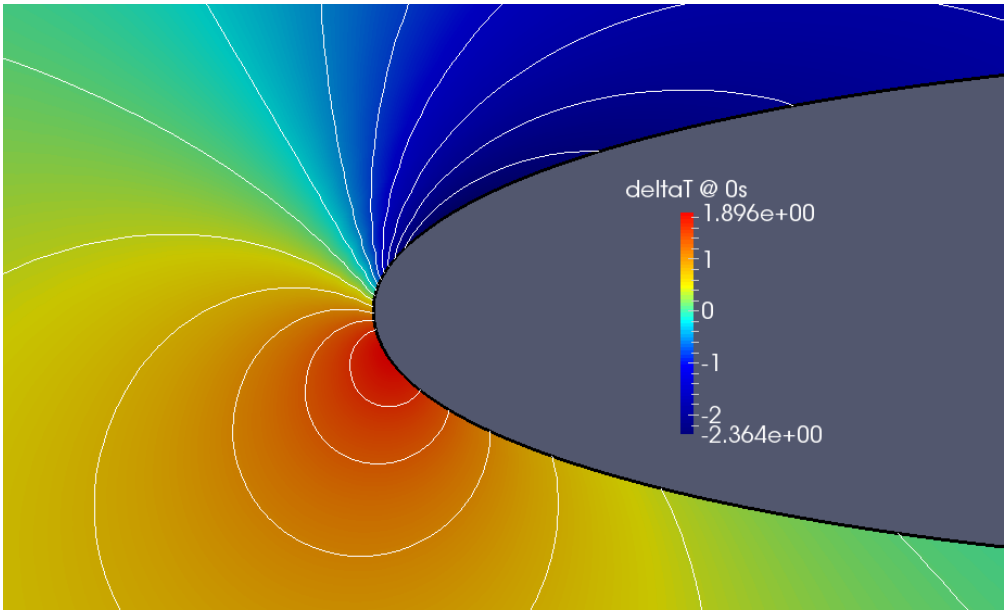

(b) ΔT field at 0 s

Figure 4.3: Flow field and the corresponding ΔT field after the reconstruction of the temperature field computed at 0 seconds.

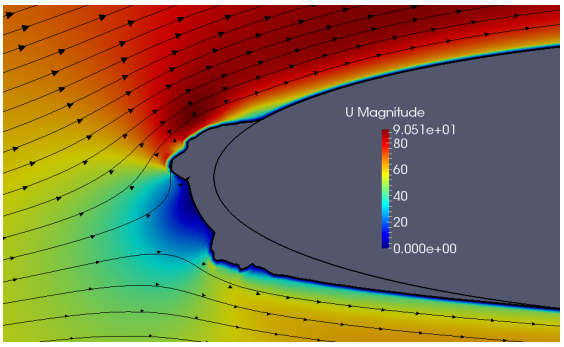

(a) Flow field at 360 s

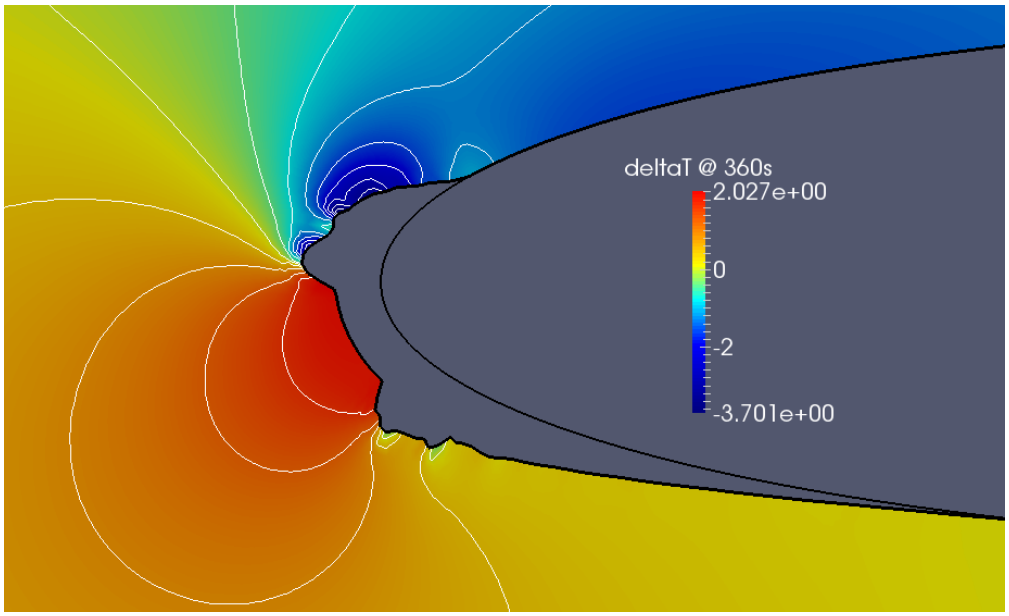

(b) ΔT field at 360 s

Figure 4.4: Flow field and the corresponding ΔT field after the reconstruction of the temperature field computed at 360 seconds.

Chapter 5

Numerical simulations

In this chapter the ice accretion software used for the simulations is introduced and exemplary bi-dimensional simulations are performed and discussed in order to highlight the behaviour of the unsteady model introduced in Ch. 3 and the advantages introduced by the use of the local temperature.
In the first sections the functioning and the set up of the aerodynamic solver, the icing solver and the mesh deformer are briefly introduced, whereas in § 5.2 the results of the simulations are discussed and compared with the respective experimental cases found in literature.

As an improvement over the previous version of `PoliMIce`, a new mesh deformation procedure based on the Shepard's interpolation algorithm is developed and implemented in § 5.1.4.

5.1 Structure of the icing suite PoliMIce

An icing software is generally composed by several modules each one specialized to solve a different aspect of the problem. In Fig. 5.1 is shown the flowchart of the PoliMIce [1] icing suite in use. The suite it composed by:

- **The aerodynamic solver**. It is the part in charge of the computation of the aerodynamic field and the particle tracking of the droplets in order to define their impact points on the surface and, consequently, the collection efficiency. For this purpose, the `OpenFOAM®` suite is used.
- **The icing solver**. It is the core of the icing code; it implements the icing models discussed before (§ 2.1, § 2.2.2 and Ch. 3) and provides the ice thickness and its final shape. For this purpose, the `PoliMIce` icing code developed here at Politecnico di Milano is used.

[1] A clarification is needed: in this section the name PoliMIce is used to indicate either the complete icing suite and the ice accretion code because of its key role within the suite. For clarity, "`PoliMIce`" is used to refer to the icing solver, whereas "PoliMIce" represents the complete suite.

- **The mesh deformer**. This is a fundamental tool that deforms the mesh around the surface to freeze in order to follow the evolution of the growing ice. In this work it has been developed a code based on the Shepard's method, an interpolation method which belongs to the *Inverse Distance Weighted* (IDW) methods.

Among these parts, an interface is needed to let the different software communicate to each others. In the following sections these parts are analysed paying particular attention to their set-up (boundary conditions, parameter setting,...).

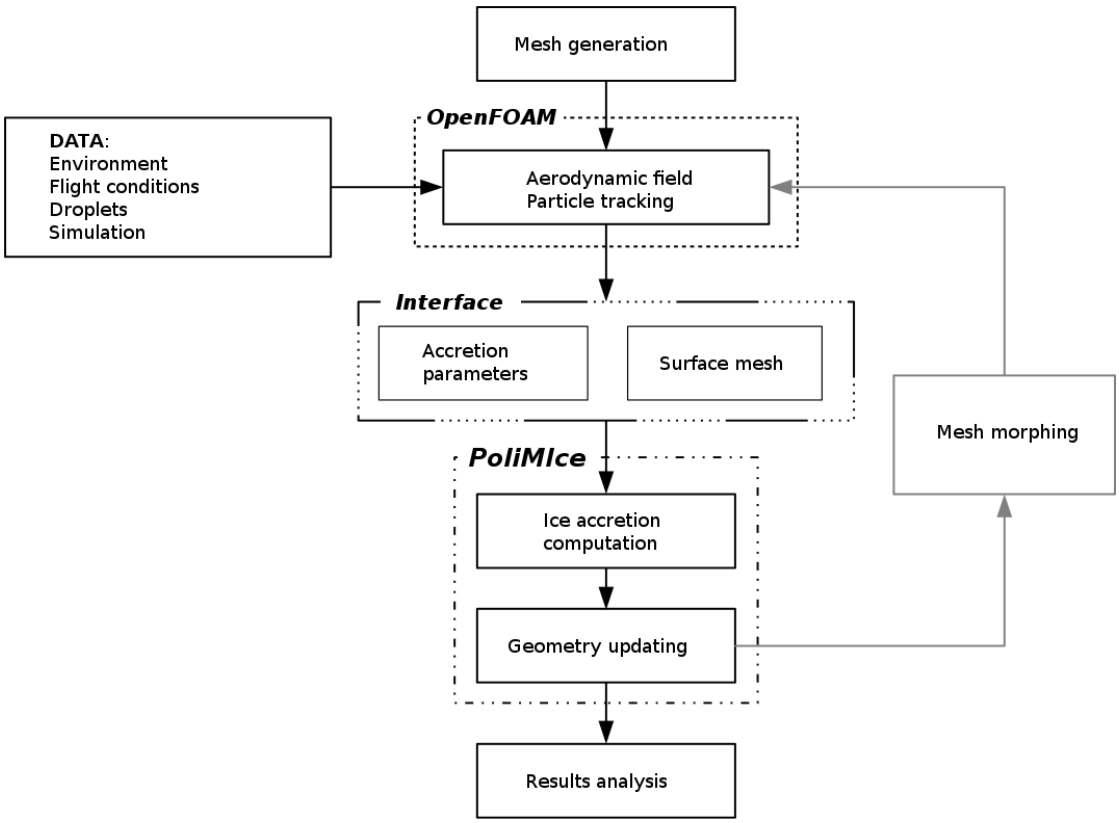

Figure 5.1: Block diagram illustrating the flowchart of the icing suite in use.

The total simulation time is subdivided into sub-intervals and the loop shown in Fig. 5.1 is executed until the final time is reached. During each loop the `OpenFOAM` solver computes the aerodynamic flow filed and the particle tracking, then the PoliMIce accretes the ice and at the end, the mesh is deformed and arranged for the next loop by the mesh deformer. The aerodynamic field around the body is considered to be the same during the chosen sub-time interval, so the field is lead to convergence towards a steady-state solution and therefore a full-unsteady aerodynamic simulation is not needed.

5.1.1 Aerodynamic solver: OpenFOAM® – `SimpleFoam`

`OpenFOAM` (Open Field Operation and Manipulation) is a free, open source CFD software package widely used for solving fluid flows involving chemical reactions, turbulence and heat transfer.

The aerodynamic solver used to perform the simulation in §. 5.2 is the `SimpleFoam` solver coupled with the Spalart-Allmaras turbulence model. `SimpleFoam` is a steady-state solver for incompressible, turbulent flow. It computes the flow field solving the steady-state RANS equations with a finite volume discretization and it is based on the SIMPLE algorithm (*S*emi-*I*mplicit *M*ethod for *P*ressure-*L*inked *E*quations). This is an iterative algorithm which starting from an initial guess, corrects the values of the pressure in order to satisfy the incompressible constrain. In the present work, the convergence of the algorithm is evaluated by the convergence of the aerodynamic coefficients C_d and C_l. For a more detailed explanation of the `SimpleFoam` algorithm see Ref [30].

The turbulence model

The Spalart-Allmaras model is a one-equation turbulence model widely used in aerodynamic applications because of its ability to dealt with separate flows. It solves the transport equation for the turbulent viscosity $\tilde{\nu}$ which is obtained from the equation of the turbulent viscosity ν_t. The Spalart-Allmaras model implemented in `OpenFOAM` follows the formulation proposed in Ref. [31] which is slightly different from the original Spalart-Allmaras formulation [32] because of a different treatment of the boundary conditions. For a deeper explanation o f the model refer to Ref. [32] and Ref. [31].

The boundary conditions

The boundary conditions imposed in the simulations involve the velocity $\boldsymbol{u}$, the pressure P, the turbulent viscosity ν_t and the variable $\tilde{\nu}$ for the Spalart-Allmaras turbulence model.
The velocity and the pressure values are taken from the reference cases chosen from literature, whereas the value of ν_t and $\tilde{\nu}$ are more difficult to be obtained and they usually come from empirical or semi-empirical relations. Fig. 5.2 and Tab. 5.1 show the domain and the boundary conditions implemented in `OpenFOAM`.

Suitable values for the variables used in the Spalart-Allmaras model are:

$$\begin{aligned} &\bullet \quad \tilde{\nu}_{\text{wall}} = 0 \\ &\bullet \quad 3\,\nu_{t_\infty} < \tilde{\nu}_\infty < 5\,\nu_{t_\infty} \end{aligned} \tag{5.1}$$

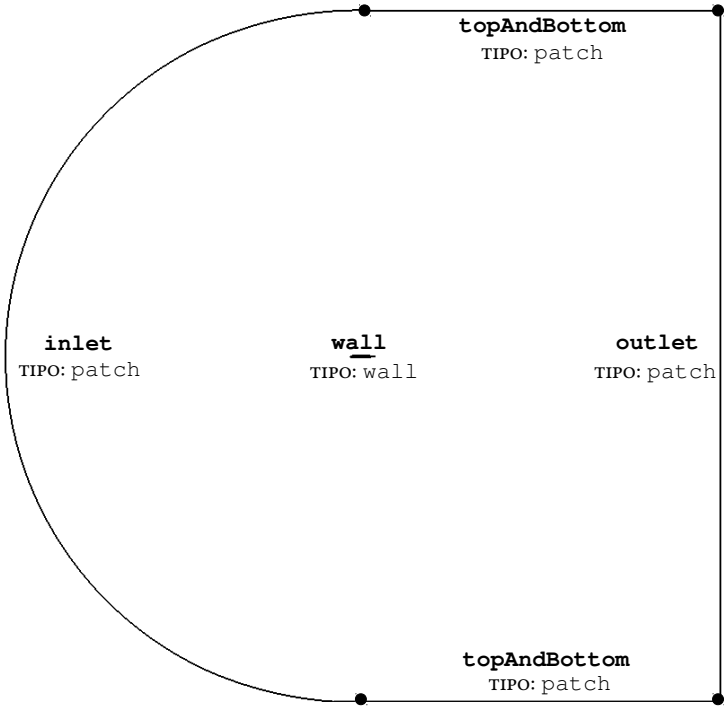

Figure 5.2: Computational domain.

Boundary	U	p	nuTilda	nut
inlet	freeStream uniform $(V_\infty \cos\alpha \;\; 0 \;\; V_\infty \sin\alpha)$	freeStreamPressure	freeStream uniform $\tilde{\nu}_\infty$	freeStream uniform $\nu_{t\infty}$
outlet	freeStream uniform $(V_\infty \cos\alpha \;\; 0 \;\; V_\infty \sin\alpha)$	freeStreamPressure	freeStream uniform $\tilde{\nu}_\infty$	freeStream uniform $\nu_{t\infty}$
topAndBottom	freeStream uniform $(V_\infty \cos\alpha \;\; 0 \;\; V_\infty \sin\alpha)$	freeStreamPressure	freeStream uniform $\tilde{\nu}_\infty$	freeStream uniform $\nu_{t\infty}$
wall	fixedValue uniform $(0 \;\; 0 \;\; 0)$	zeroGradient	fixedValue uniform 0	*Wall function* uniform 0

Table 5.1: Boundary conditions used for the OpenFOAM simulations.

Following [33] or [34], the value of $\tilde{\nu}_\infty$ used in this work are:

$$\begin{aligned} &\bullet \quad \tilde{\nu}_\infty = 0.000342929 \cdot V_\infty c \\ &\bullet \quad \nu_{t_\infty} \approx \frac{\tilde{\nu}_\infty}{24} \end{aligned} \tag{5.2}$$

where c is the airfoil chord length. At the wall $\tilde{\nu}_{\text{wall}}$ is set to zero and a *wall function* for ν_t is used in order to speed up the computation.

5.1.2 Particle tracking: OpenFOAM® – `uncoupledKinematicParcelFoam`

The particle tracking method used in the following simulation is based on a Lagrangian approach. This model perform a force balance over each single droplet assuming that

- the droplets are spherical and no collisions are possible,
- the forces acting on the droplets are only the gravity, the buoyancy forces and the aerodynamic drag,
- the droplets does not influence the aerodynamic field, they are only transported by the flow field.

The equation of motion of the droplets is based on the following force equilibrium

$$m_d \frac{\mathrm{d}\vec{u}_d}{\mathrm{dt}} = \vec{F}_{aero} + \vec{F}_g \tag{5.3}$$

where the subscripted index d stands for the droplets. A more detailed explanation is resent to Ref. [3] or Ref. [35].
The importance of an accurate evaluation of the droplets trajectories is reflected into an accurate definition of the collection efficiency parameter (β) which is a fundamental parameter governing the ice accretion process.

The computation of the droplets trajectories is performed using the `uncoupledKinematicParcelFoam` solver implemented in `OpenFOAM`. This solver perform a numerical integration of the equation of motion starting from an initial cloud of droplets specified into a setup file. Droplets are treated as a passive scalar, so they do not interact with the surrounding aerodynamic field and when the simulation time is over the solver returns the wall cells where the droplets have collided. At this point these informations pass to the interface which computes the collection efficiency β.
An example of the `uncoupledKinematicParcelFoam` application is shown in Fig. 5.3.

5.1.3 Ice accretion solver: `PoliMIce`

The `PoliMIce` code is the core of the icing suite. It receives as input the aerodynamic data and the particle tracking results computed by `OpenFOAM` and provides the ice thickness and shape after the accretion time-step. Reasonable values for the time-step is around 10 seconds.
The `PoliMIce` code can performs simulations using all the models introduced before except the Messinger's one (Myers model, modified Myers model, full-unsteady model) associated to the upstream static temperature T_∞ or the local temperature T_{local}. In this way it is easy to perform some comparisons between the models.

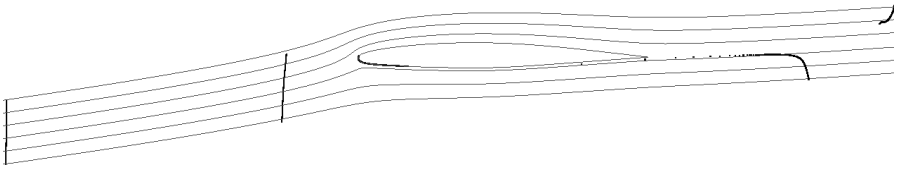

(a) Droplets positions at different times: $t = 0.01\,s$, $t = 0.02\,s$ and $t = 0.04\,s$

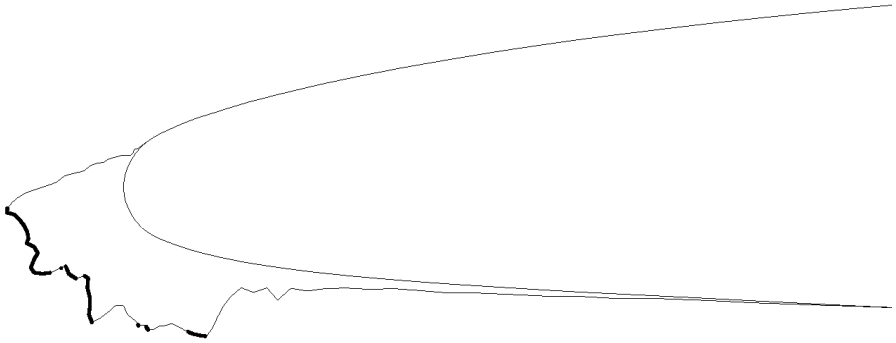

(b) Impact limits over an iced airfoil

Figure 5.3: Example of droplets trajectories and impact limits in a bi-dimensional case.

5.1.4 Mesh deformer: Shepard method

One of the most relevant problem in mesh warping concern the ability of the code to take into account punctual deformations without "breaking" the mesh. In many cases (i.e. in Fig. 5.4) the appearance of horns and irregular icing structures bring the warping process to stretch some portions of the mesh too much or to penetrate some cells into each others.

In this work an Inverse Distance Weighting method (IDW) is used due to its robustness in these situations.

The algorithm

Shepard's algorithm [36] belongs to the IDW methods, a class of interpolation methods based on a weighted average process and generally used to interpolate bi or tridimensional spatial data. The weights appearing in the average process are the inverse of the distances between the two considered points, therefore the nearest points to the unknown have the greatest influence on its finale value.
Given a known discrete field U, the interpolation of the variable $u(\mathbf{x})$ at the generic point $\mathbf{x}$ depends on the inverse of the distance of the surrounding N points. Each point is a known sample $u_i = u(x_i)$ of the U field.

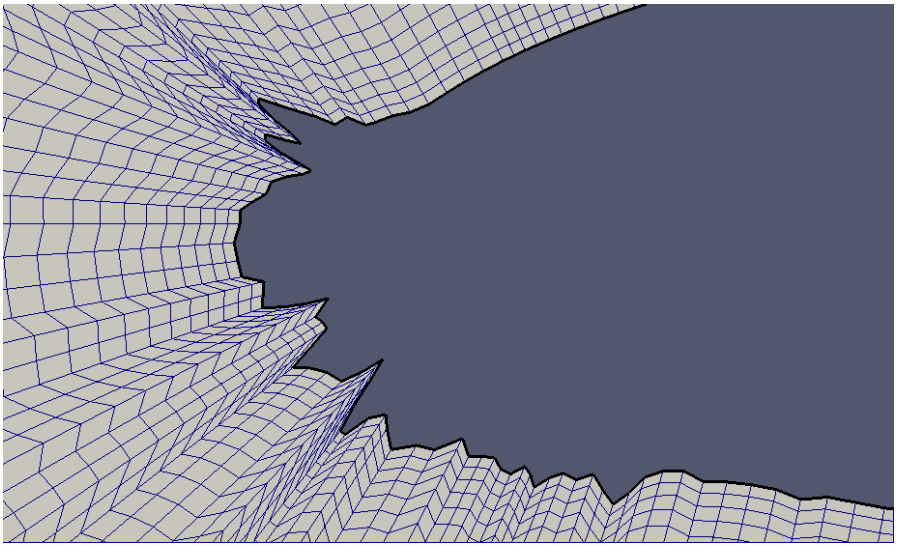

Figure 5.4: Example of a wrecked mesh in the case of punctual deformations. The skewness and the aspect ratio of many elements are not appropriate for a CDF computation.

The interpolation equation is:

$$u(\mathbf{x}) = \begin{cases} \dfrac{\sum_{i=1}^{N} w_i(\mathbf{x})\, u_i}{\sum_{i=1}^{N} w_i(\mathbf{x})}, & \text{if } d(\mathbf{x}, \mathbf{x}_i) \neq 0 \\ u_i, & \text{if } d(\mathbf{x}, \mathbf{x}_i) = 0 \end{cases} \tag{5.4}$$

where the weights are $w_i(x) = \dfrac{1}{d(\mathbf{x}, \mathbf{x}_i)^p}$ and the distance between the points x and x_i is $d(\mathbf{x}, \mathbf{x}_i)$.
The exponent p in the weight relation increases (or decreases) the influence of the closest values to the interpolated point. The higher is p, the most influence the nearest points have.

In order to speed up the code execution, a modified version of the weight is used. In this formulation only the points within a certain distance R from $\mathbf{x}$ are taken into account for the weight computation:

$$w_i(\mathbf{x}) = \left(\frac{\max(0, R - d(\mathbf{x}, \mathbf{x}_i))}{R d(\mathbf{x}, \mathbf{x}_i)} \right)^2 \tag{5.5}$$

An example of the reliability of the algorithm can be seen in Fig. 5.5 where a local deformation does not produce a singularity but it is "absorbed" and spread to a group of contiguous points.

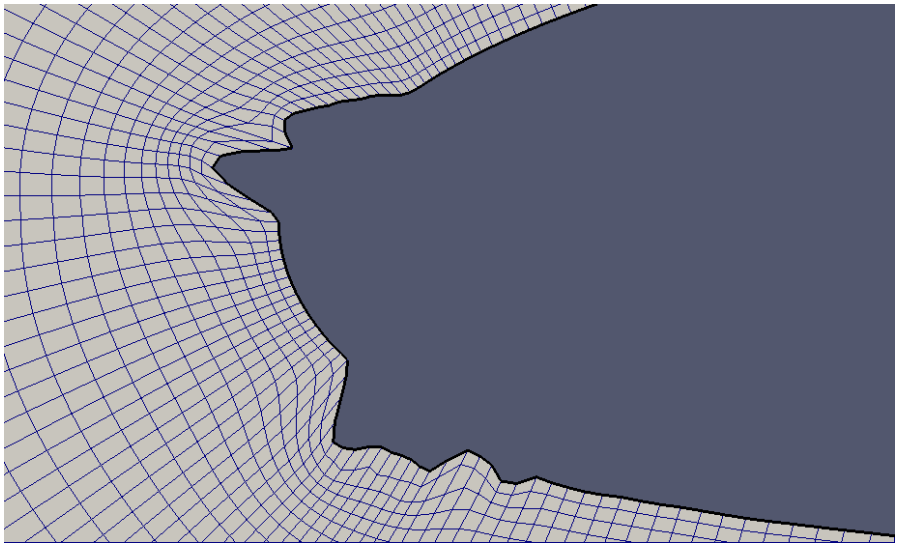

Figure 5.5: Example of the application of the Shepard's method in a case with punctual deformations. The quality of the resulting mesh is suitable for an aerodynamic simulation.

5.2 Test cases

Exemplary test cases regarding both rime and glaze ice accretion over two-dimensional airfoil are now discussed.

Test conditions were chosen with the aim of verify and affirm the critical aspect of the novel icing model. In particular atmospheric temperature for the first test case in § 5.2.1 is slightly less than the ice melting point thus being representative of conditions where ice grows mostly as *glaze* type. Test case showed in § 5.2.2 is instead exemplifying the opposite circumstances, i.e. *rime*-ice accretion is prevailing over the airfoil. Further details about the following test cases, as well as informations regarding the experimental set up can be found in Ref. [8] and Ref. [9]. Results are compared against prediction from other ice accretion solvers and against experimental results.

In the following sections, the PoliMIce model refers to the complete new model with the unsteady exact temperature profile, the correction of the local temperature and the introduction of the $\dot{m}_{in}^{w}$. The Myers model is instead the pure model without any correction.

5.2.1 Glaze-ice test case

The main goal of this simulation is to show the benefits of the introduction of the unsteady exact temperature profile within the ice layer, this modification is indeed applicable only during the glaze-ice accretion. The reference case is the number 31 in Ref. [8] and it provides favourable conditions for the glaze-ice accretion since the beginning of the

simulation. Furthermore, the use of the modified version of the rime limit thickness accelerate the rime-glaze transition and the resulting ice is completely glaze.
The atmospheric conditions for this test case are reported in Tab. 5.2.

Airfoil	NACA 0012	[–]
$\boldsymbol{\alpha}$	4	[deg]
$\mathbf{V_\infty}$	58.1	[m/s]
$\mathbf{T_\infty}$	269.1	[K]
$\mathbf{P_\infty}$	95600	[Pa]
LWC	1.3	[g/m^3]
MVD	20	[μm]
c	0.53	[m]
time	480	[s]

Table 5.2: Simulation data for the glaze-ice test case

Results obtained using the original Myers' model, the PoliMIce model and the experimental shape taken from Ref. [8] are compared in Fig. 5.6. The total exposure time is 480 s and the flow-field update interval is 10 s.

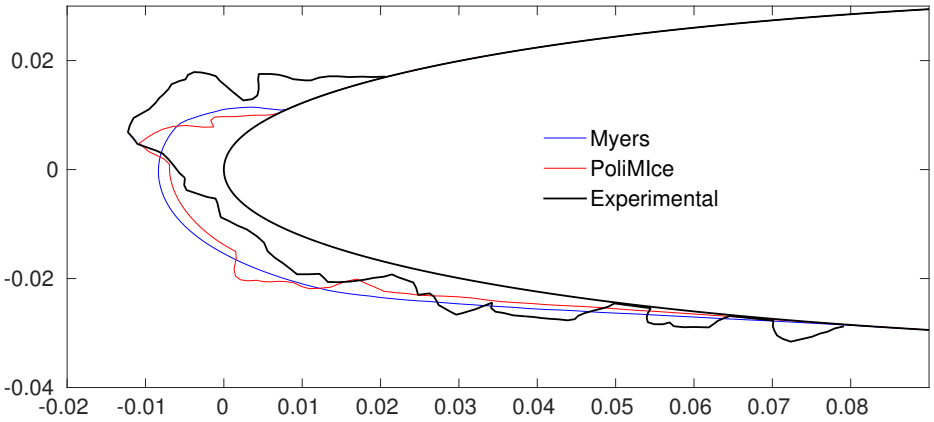

Figure 5.6: NACA0012: comparison of PoliMIce predictions with numerical results for the original Myers' model and experimental ice shape from Ref. [8] for the glaze ice case in Tab. 5.2.

Experimental results evidence a large ice structure one the upper portion of the leading edge and ice formation on the lower portion that extends for 0.08 m (airfoil chord is 0.53 m). The Myers' model predicts a quite regular and smooth shape and the system of highly complex ice structures is loosely represented. The proposed model instead match more closely the experimental result and it predicts the occurrence of the

ice structure protruding from the leading edge. The size of the latter one is however poorly captured and the ice thickness at the stagnation point is sightly closer to the experimental results but it is however over-estimated.

With particular reference to the estimation of the ice thickness in the close proximity of the stagnation point, both improvements that were introduced with respect to the Myers' model – the more accurate description of the heat diffusion problem through the ice layer and the inclusion of a variable temperature profile within the boundary layer – contribute to match the experimental results more closely. The ability of representing irregular structures is possibly due to the inclusion of the $\dot{m}_{in}^{w}$ term in the rime ice accretion and the use of the local temperature field nearby the airfoil. Fig. 5.7 shows a comparison between the unsteady model with and without the contribution of the $\dot{m}_{in}^{w}$. The air temperature is referred to its local value.

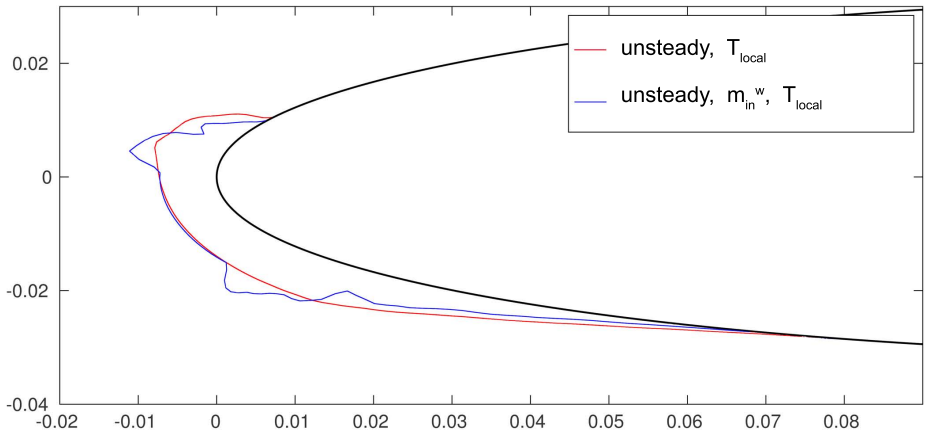

Figure 5.7: NACA0012: comparison of the unsteady model with and without the contribution of the $\dot{m}_{in}^{w}$ in the mass balance. The air temperature is referred to its local value.

Ice is known to grow first as *rime* ice and then, after the thickness exceeds the B_g value, to continue growing as glaze ice: simulation data show that the B_g function has a relative minimum in the region close to the stagnation point. This is possibly directly dependent on the collection efficiency distribution which, on the other hand, reaches its maximum in the same cells. Then the higher amount of water hitting this portion of the surface causes *glaze* ice to appear first and hence the liquid film starts flowing over the airfoil towards the trailing edge along both the upper and the lower side. The film is driven by the wall shear stress, under the action of the external air stream. So water flows into the neighbouring cells that, due to their position along the airfoil chord, are layered by a lower value of β and T. In this cells the B_g is then higher and rime ice, which is faster than glaze, grows for a longer time thus producing the double-horn irregular shape.

Fig. 5.8(a) and Fig. 5.8(b) shows the ice shapes predicted by the Myers and the PoliMIce model, respectively, in the case of uniform or local air temperature. The blue line shows the numerical ice shapes obtained with a uniform temperature field surrounding the wing. The uniform temperature is equal to the free stream one. On the other hand, the red line reports the numerical ice shape obtained including the effects of the local temperature field near the surface. This local value is obtained from the aerodynamic solver following the isentropic relations recalled in Ch. 4. The inclusion of this simple correction is found to be beneficial for predicting of the ice thickness at the stagnation point and also the ice structure in the upper portion of the leading edge. As shown in Fig. 4.3 and Fig. 4.4 (in Ch. 4), the temperature at the stagnation point is higher than the free stream one, so the process described before regarding the accretion of the horns is facilitated thanks to the lower quantity of water that freezes at this point and the corresponding higher quantity that can flow aft. Comparing Fig. 5.7 and Fig. 5.8(a) it is observed that the only temperature correction is not sufficient to provide the irregular shape but the combination with the inclusion of the $\dot{m}_{in}^{w}$ gives better results.

Fig 5.9 shows the comparison between the simulation performed with the linear temperature profile within the ice and the exact unsteady one. The two lines are almost overlapped, so the correction of the unsteady temperature is not so relevant in this case. The zoom on the first time steps near the stagnation point shows that at the beginning of the icing process the exact temperature profile predict a slightly more thick ice, then the accretion rate reduces and the trend is inverted. At the end of the simulation the ice predicted by the Myers model is slightly thicker than the unsteady one and from 200 seconds on, this difference is maintained constant. This confirm that the unsteady correction may be more useful during the initial transitory. Graph in Fig. 5.10 represents the difference of the two ice thickness in the first 200 seconds of accretion.

In conclusion, Fig. 5.11 reports a comparison of the present numerical results with those obtained by the LEWICE, ONERA and TRAJICE icing sofwtare. All these software overestimate the location of the ice-free region in the upper portion of the airfoil, which is however underestimated by the PoliMIce software. The LEWICE, ONERA and TRAJICE software also deliver a better estimate of the ice thickness at the stagnation point with respect to the present model. The ice shape predicted by the three software is very smooth, which possibly corresponds to the earlier occurrence of glaze ice.

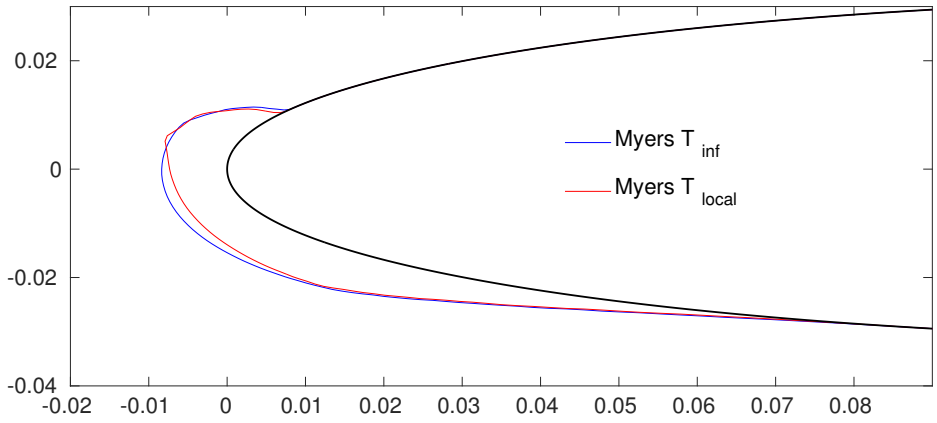

(a) Glaze-ice test for the NACA 0012 airfoil (Tab. 5.2). Comparison of numerical results obtained from the Myers' model by assuming a uniform air temperature equal to the free stream temperature and by including the local temperature field obtained by CFD simulations.

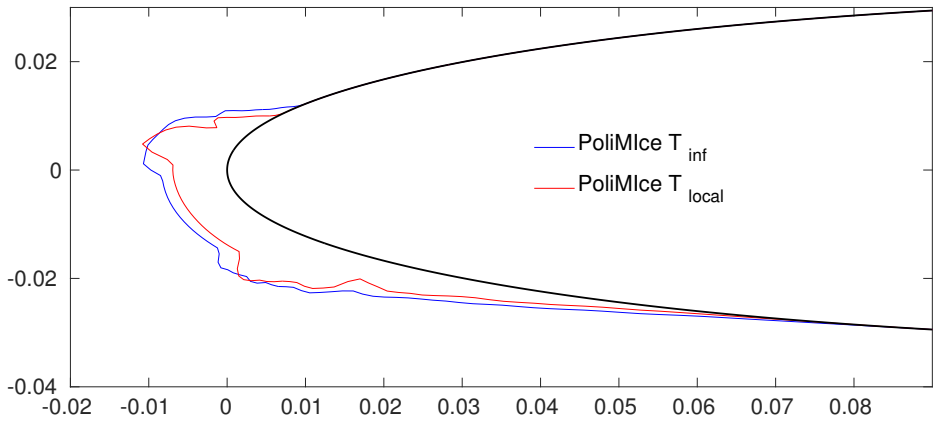

(b) Glaze-ice test for the NACA 0012 airfoil (Tab. 5.2). Comparison of numerical results obtained from the new complete unsteady model by assuming a uniform air temperature equal to the free stream temperature and by including the local temperature field obtained by CFD simulations.

Figure 5.8: Glaze-ice test for the NACA 0012 airfoil.

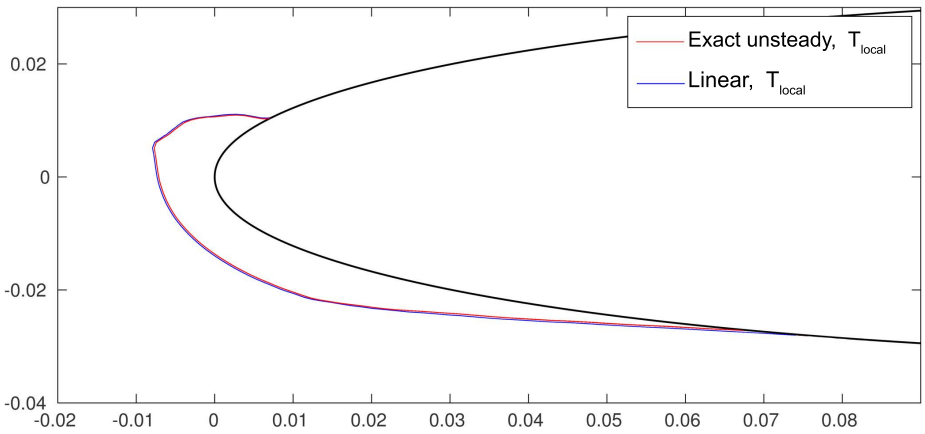

Figure 5.9: NACA0012: comparison between the unsteady model and the linear Myers model. The air temperature is referred to its local value.

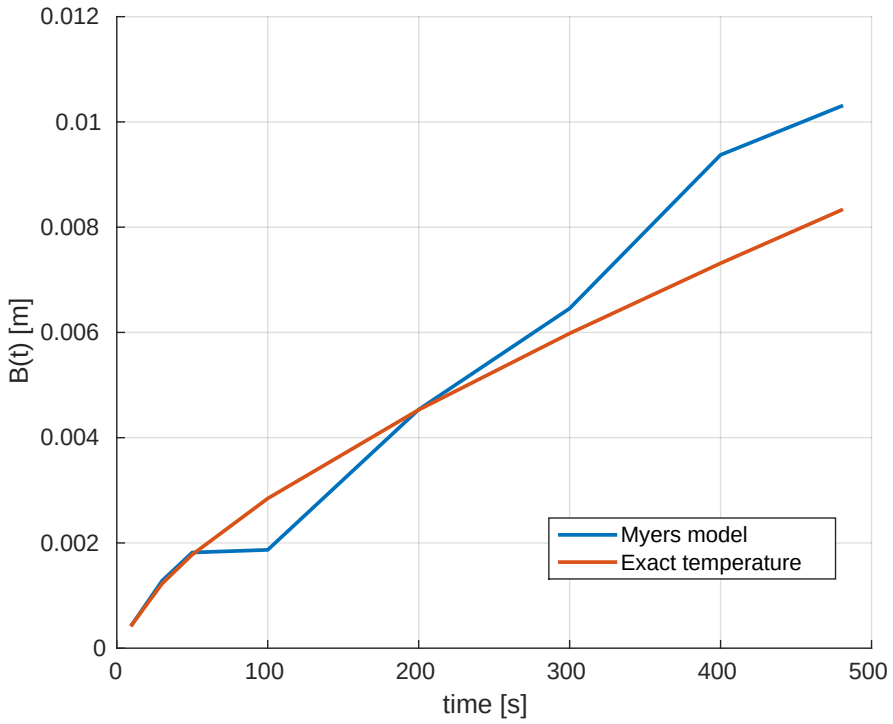

Figure 5.10: NACA0012: comparison of the unsteady model with and without the contribution of the $\dot{m}_{in}^{w}$ in the mass balance.

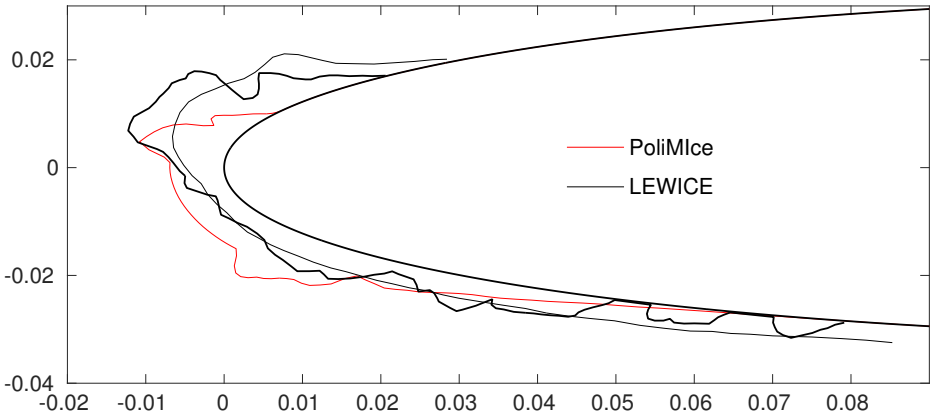

(a) LEWICE

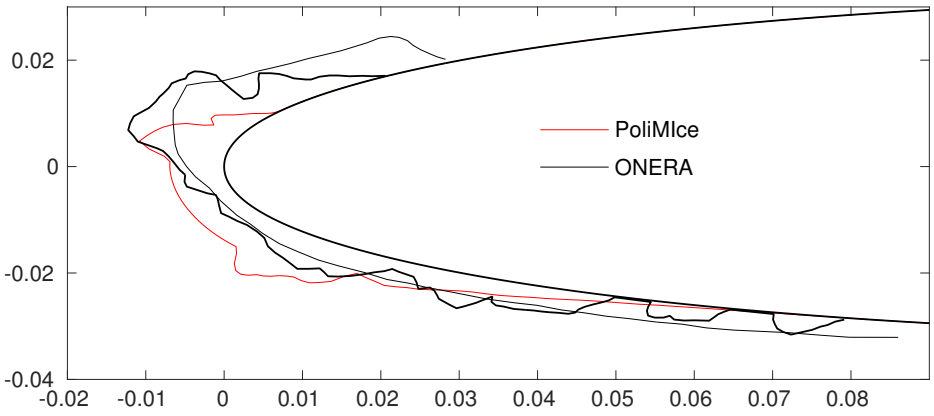

(b) ONERA

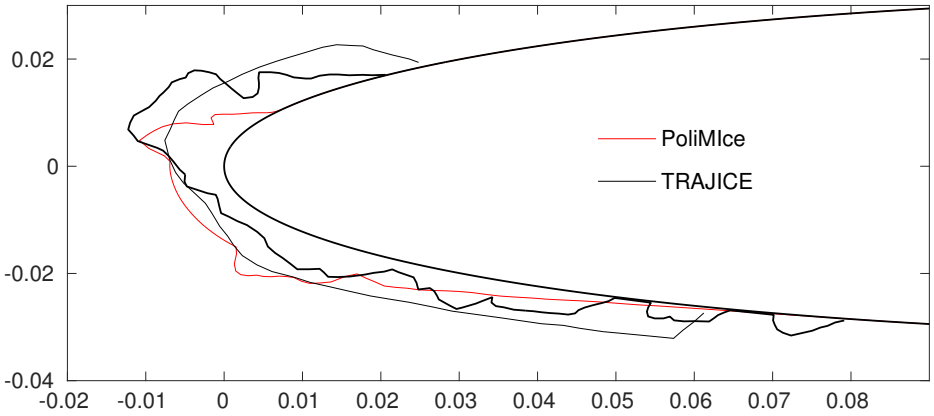

(c) TRAJICE

Figure 5.11: NACA0012: comparison of PoliMIce predictions with numerical results for the LEWICE, ONERA and TRAJICE software in the glaze ice case in Tab. 5.2. In all plots, the thick black line is the experimental ice shape reported in Ref. [8].

5.2.2 Rime-ice test case

The test case presented in this section corresponds to the ice accretion an aircraft may experience while flying at very low temperature conditions for a significant time. The test case conditions were chosen from Ref. [9] mainly because of its low values of temperature and LWC which are indexes of a possible rime-ice accretion. The aim of this simulation is indeed to investigate how the novel model behaves in representing the final ice shape in rime-ice conditions and in particular the attention is focused on the local temperature correction. The atmospheric conditions of the simulation are summarized in Tab. 5.3.

Airfoil	GLC 305	[–]
$\boldsymbol{\alpha}$	1.5	[deg]
$\mathbf{V_\infty}$	128.6	[m/s]
$\mathbf{T_\infty}$	262.9	[K]
$\mathbf{P_\infty}$	125484	[Pa]
LWC	0.43	[g/m^3]
MVD	20	[μm]
c	0.91	[m]
time	360	[s]

Table 5.3: Simulation data for the rime-ice test case

Fig. 5.12 shows the comparison between the PoliMice complete model, the Myers model and the experimental results taken from the aforementioned report. The experimental result evidence the accretion of two horns protruding towards the direction of motion and separated by a region of low ice thickness in the proximity of the stagnation point. The ice accretion is not spread along the wing but it grows near the leading edge due to its rime characteristics and the small angle of attack produce a slightly asymmetry, indeed the upper horn is slightly longer than the other.

The main differences between the Myers model and the PoliMIce complete model is the ability of the PoliMIce model to capture the horns formations and to better represent the thickness at the stagnation point. The Myers model predicts a smooth shape with its maximum thickness at the stagnation point where the experimental result predicts its minimum value. PoliMIce instead is more accurate even if the upper horn accretion direction is slightly different from the experimental one and the the thickness at the stagnation point is over-estimated respect to the experimental accretion. This improvements is produced by the combination of the effects of the local temperature and the introduction of the $\dot{m}_{in}^{w}$. The temperature at the stagnation point is higher than the surrounding regions, so the ice grows less and more water appears. This water then flows away entering in the regions where the temperature is locally low and freezes. Comparing Fig. 5.14(a) and Fig. 5.14(b) it is interesting to observe that the the two modifications introduced separately does not provide a such good result but affect only the ice thickness at the stagnation point. The Fig. 5.14(a) indeed does not have the $\dot{m}_{in}^{w}$ contribution and

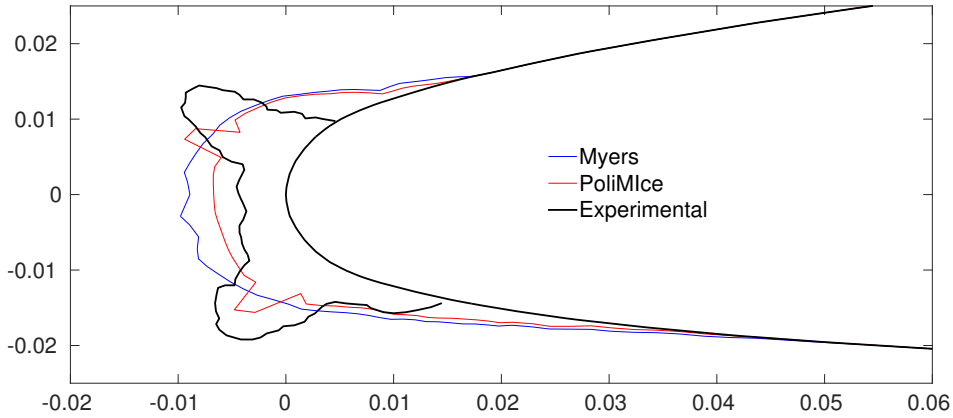

Figure 5.12: GLC 305: comparison of PoliMIce predictions with numerical results for the original Myers' model and experimental ice shape from Ref. [9] for the rime ice case in Tab. 5.3.

the horns does not appear also with the local temperature correction.

The results provided by the exact unsteady model (without the $\dot{m}_{in}^{w}$ contribution) and the Myers model are expected to be the same because of the preponderance of the rime-ice accretion. Fig. 5.13 illustrate indeed the likeness of the two curves.

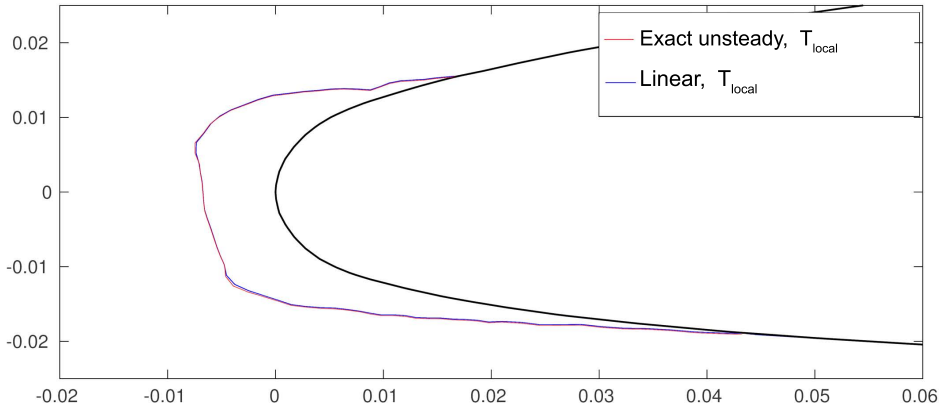

Figure 5.13: GLC 305: comparison of the unsteady model with and without the contribution of the $\dot{m}_{in}^{w}$ in the mass balance.

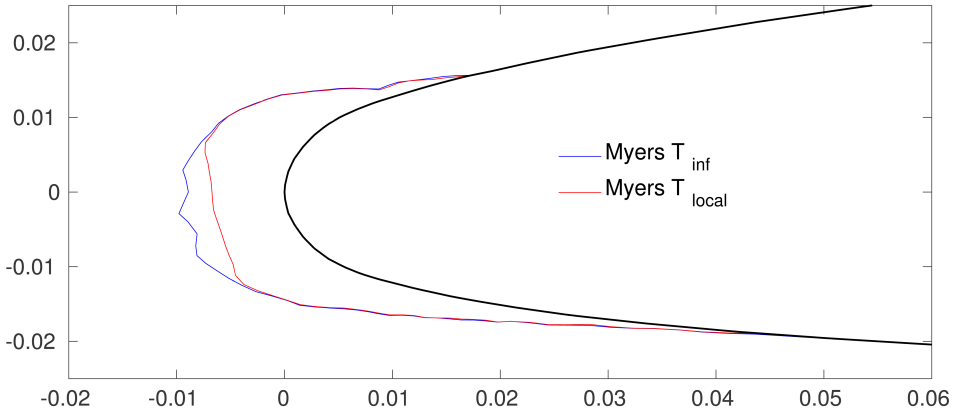

(a) Myers

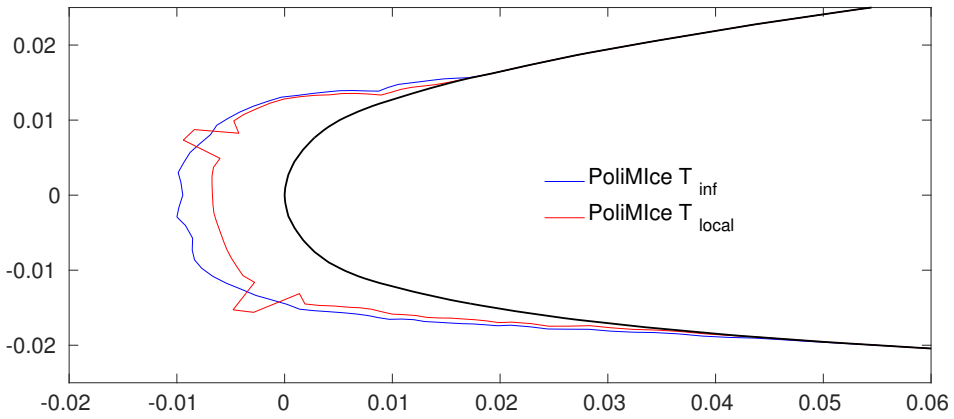

(b) PoliMIce

Figure 5.14: Rime ice test for GLC 305 airfoil (Tab. 5.3). Comparison of numerical results obtained by assuming a uniform air temperature equal to the free stream temperature and by including the local temperature field obtained by CFD simulations, for the Myers' and the PoliMIce models.

Chapter 6

Conclusions and future works

In the present thesis, a novel unsteady model for ice accretion over aircraft flying in icing conditions was derived. The new model is based on the exact solution of the unsteady Stefan problem and it represents an improvement over current ice accretion models, including the well-known Myers model, which are based on the assumption that the temperature profile within the ice layer is constant over time. To this purpose, the exact solution for the unsteady temperature profile was derived for the first time and applied to ice accretion simulations over two-dimensional airfoils. The exact solution for the temperature profile is as follows:

$$T_{(z,t)} = T_{\text{wall}} + (T_{\text{freezing}} - T_{\text{wall}}) \frac{\text{erf}\left(\dfrac{z}{2\sqrt{\alpha_i t}}\right)}{\text{erf}(\lambda)}$$

where the parameter λ,

$$\lambda = \frac{B(t)}{2\sqrt{\alpha_i t}}$$

is computed by iterating starting from the Stefan condition.

A local correction to the air temperature is also included to account for the dependence of the outer (air) temperature on the flow field, whereas in the Myers model the outer air temperature is assumed to be constant and equal to its free-stream value. The local value of the temperature outside the boundary layer is computed from the free-stream temperature and from the local velocity by assuming an isentropic transformation.

A novel mesh deformation procedure was also developed and implemented in the PoliMIce suite, which is based on the Shepard interpolation method. The new mesh deformation algorithm represents an improvement over the original one that was based on the representation of the grid as elastic continuum.

Numerical simulations of two-dimensional airfoil in icing conditions were carried out to assess the correctness of the new model and its behaviour in rime and glaze ice conditions. Numerical simulations relied upon the open-source `OpenFOAM` suite for the computation of the aerodynamic flow field and of the droplet trajectories.

Simulations performed in Ch. 5 showed that the contributions of the unsteady terms is not significant in the considered cases, apart during the initial transitory. In this lapse, the derivative of the temperature at the wall is higher than the one calculated by the Myers model. This behaviour is possibly important in the design of an anti-icing system for the evaluation of the heat flux to apply at the wall. On the other hand, the introduction of the local temperature gives more accurate results in the ice shape prediction. After this modification, the ice shapes resulting from the simulations are generally more irregular with the appearance of "horn" structures. In the rime case it is also observed a more accurate prediction of the ice thickness at the stagnation point.

The present work highlighted the need of a more deeper investigation on the conditions in which the unsteady effects become relevant, for example super-cooled large droplets (SLD) conditions or conditions in which the aircraft quickly reduces its altitude. The icing model could be further modified in order to take into account the presence of an anti-icing system.

An interesting area for further investigation is the modelling of the flow of surface water. In the current implementation the superficial water is simply modelled as a plane surface with a fixed height of $1/10$ mm where the water flows toward the direction of the wall shear stress but it is not affected by its intensity. Under this assumption, it is not possible neither the accumulation nor the reduction of the water content in a given portion of the surface where the shear stress changes module or direction. A possibility is to develop a multidimensional model of the shallow-water like the one reported in Ref. [22]. Another improvement regarding the water layer is the introduction of a model for the splash of the droplets when they impact the surface and the introduction of the possibility for the water layer to separate from the body. In this way a consequently re-introduction of the water in the airflow is possible. In order to increase the accuracy of the ice shape prediction, a multi-zone model could also be developed in order to take into account the different surface roughness conditions along the surface produced by rivulets, beads and runback-ice like in Ref. [19].

Bibliography

[1] Icing conditions in flight. http://www.pilotfriend.com/safe/safety/icing_conditions.htm.

[2] De-icing training and innovations. http://training.deicinginnovations.com/.

[3] Gent R. W., Dart N. P., and Cansdale J. T. Aircraft icing. *Philosophical Transactions of The Royal Society A*, 358:2873–2911, 2000.

[4] NASA Glenn Research Center. http://www.nasa.gov/centers/glenn/home/index.html.

[5] NASA.gov. http://www.nasa.gov/offices/oct/home/tech_life_kestrel_prt.htm.

[6] Aviation troubleshooting. http://aviationtroubleshooting.blogspot.it/2011/01/future-of-deicing-technology-and.html.

[7] Messinger B. L. Equilibrium temperature of an unheated icing surface as a function of air speed. *Journal of the Aeronautical Sciences*, pages 29–42, January 1953.

[8] Wright W. B., Gent R. W., and Guffond D. DRA / NASA / ONERA, Collaboration on icing research (Part II: prediction of airfoil ice accretion). *NASA/CR 202349*, 1997.

[9] Jr Addy H. E., , Potapczuk M. D., and Sheldon D. W. Modern Airfoil Ice Accretions. Technical Memorandum 107423, NASA, 1997.

[10] Linacre E. and Geerts B. Cloud liquid water content, drop sizes, and number of droplets. http://www-das.uwyo.edu/~geerts/cwx/notes/chap08/moist_cloud.html, 1999.

[11] Myers T. G. Extension to the messinger model for aircraft icing. *AIAA Journal*, 39(2):211–218, February 2001.

[12] Jones S. M., Reveley M. S., Evans J. K., and Barrientos F. A. Subsonic aircraft safety icing study. Technical Memorandum 215107, NASA, 2008.

[13] Petty K. R. (National Transport Safety Board Aviation) and Floyd C. D. J. A statistical review of aviation airframe icing accidents in the U.S. In *11th Conference on Aviation, Range, and Aerospace Meteorology*, Hyannis, Massachusetts, 2004.

[14] Valarezo W. O. Maximum lift degradation due to wing upper surface contamination. In *Boundary-Layer Stability and transition*, Montreal, Canada: Ecole Polytechnique de Montreal, September 1993.

[15] National Transport Safety Board Aviation. In-flight icing encounter and loss of control Simmons Airlines, d.b.a. American Eagle flight 4184 avions de transport regional (ATR) model 72-212, N401AM. Accident Report AAR-96-01, NTSBA, Monroe, Michigan, July 1994.

[16] National Transport Safety Board Aviation. In-flight icing encounter and uncontrolled collision with terrains, COMAIR Flight 3272, Embraer EMB-120RT, N265CA. Accident Report AAR-98-04, NTSBA, Monroe, Michigan, January 1997.

[17] Hardy J. K. Protection of aircraft against ice. Technical Report 3380, Royal Aircraft Establishment, 1946.

[18] Langmuir I. and Blodgett K. B. A mathematical investigation of water droplet trajectories. Technical Report 5418, Army Air Forces, 1946.

[19] Fortin G., Ilinca A., Laforte J. L., and Brandi V. Prediction of 2D airfoil ice accretion by bisection method and by rivulets and beads modeling. In *41st Aerospace Sciences Meeting and Exhibit*, Reno, Nevada, January 2003. American Institute of Aeronautics and Astronautics (AIAA).

[20] A NASA guide to ground-icing and in-flight icing for pilots. `http://aircrafticing.grc.nasa.gov/courses.html`.

[21] Stefan J. Ueber die theorie der eisbil-dung im polarmeere. *Annalen Der Physik Und Chemie*, 42:269–286, 1891.

[22] Myers T. G., Charpin J. P. F., and Chapman S. J. The flow and solidification of a thin fluid film on an arbitrary three-dimensional surface. *Physics of fluids*, 14(8):2788–2803, 2002.

[23] Myers T. G. and Charpin J. P. F. A mathematical model for atmospheric ice accretion and water flow on a cold surface. *International Journal of Heat and Mass Transfer*, (47):5483–5500, 2004.

[24] Naterer G. F. Dispersed multiphase flow with air-driven runback of a liquid layer at a moving boundary. *International Journal of Multiphase Flow*, 29:1833–1856, 2003.

[25] Lamé G. and Clapeyron B. P. Mémoire sur la solidification par refroidisse-ment d'un globe liquide. *Annales Chimie Physique*, 47:250–256, 1831.

[26] Damlamian A. Some results on the multi-phase Stefan problem. *Partial Differential Equations*, 2(10):1017–1044, 1977.

[27] Garabelli M. and Gori G. PoliMIce: un ambiente di simulazione per la previsione dell'accrescimento di ghiaccio su velivoli. Master's thesis, Politecnico di Milano, 2013.

[28] Mitchell S. L. and Vynnycky M. Finite-difference methods with increased accuracy and correct initialization for one-dimensional Stefan problems. *Applied Mathematics and Computation*, 215:1609–1621, 2009.

[29] Boucìguez A. C., Lozano R. F., and Lara M. A. About the exact solution in two-phase Stefan problem. *Engenharia Térmica (Thermal Engineering)*, 6:70–75, December 2007.

[30] Patankar S. V. *Numerical Heat Transfer and Fluid FLow*. McGraw Hill, 1980.

[31] NASA Langley Research Center Turbulence Modeling Resource. `http://turbmodels.larc.nasa.gov/`.

[32] Spalart P. R. and Allmaras S. R. A one-equation turbulence model for aerodynamic flows. *Recherche Aerospatiale*, (1):5–21, 1994.

[33] Guidelines for specification of turbulence at inflow boundaries. `http://www.esi-cfd.com/esi-users/turb_parameters/`.

[34] Zocca M. Effetti di galleria nelle misure di formazione di ghiaccio su velivoli. Master's thesis, Politecnico di Milano, 2013.

[35] Silvera R. A., Maliska C. R., Estivam D. A., and Mendes R. Evaluation of collection efficiency methods for icing analisys. In *Proceedings of COBEM 2003*, São Paulo, November 2003. International Congress of Mechanical Engineering (COBEM). 17th International Congress of Mechanical Engineering.

[36] Shepard D. A two-dimensional interpolation function for irregularly-spaced data. In *Proceedings of the 1968 23rd ACM national conference*, pages 517–524. Association for Computing Machinery (ACM), 1968.